Multicomponent Copper(I) Oxide/Gold Nanoparticles and Their Assembly

Dávid Kovács

Materials Science MSc

Supervisors:

Dr. Dániel Zámbó

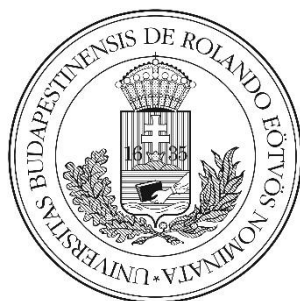*Research Fellow*

Dr. András Deák

Senior Research Fellow

Institute of Technical Physics and Materials Science

Centre for Energy Research

Internal Consultant:

Prof. Dr. Éva Kiss, *Professor Emeritus*

Eötvös Lóránd University

Eötvös Lóránd University

Faculty of Science

Budapest, 2022

Acknowledgement

First and foremost, I would like to express my deepest gratitude to Dr. Dániel Zámbó who guided me throughout the project. Thank you for the excellent guidance and support in completing this work all the time, and for giving me the opportunity to follow my research interests. No other project would have been more suitable for me. Also, thank you for the assistance in obtaining the SEM and EDS measurements.

Special thanks to Dr. András Deák for providing the facilities to perform my research. I appreciate your encouragement, and motivation throughout the course of the research. Your advice, ideas, and insights were very valuable.

I am grateful to Prof. Dr. Éva Kiss for being my adviser, and for introduced me the fascinating world of materials science. I would like to thank all my colleagues who contributed to this work, especially Dr. Dániel Péter Szekrényes, I am grateful for the time working with you. I would like to express my gratitude to all collaborators, Ottó Czömpöly for the TXRF measurements, Dr. Zsolt Endre Horváth for the XRD measurements and Dr. György Zoltán Radnóczi for HRTEM and EDS measurements.

Last but not the least, I am deeply grateful to my family for their love, kindness, care, and support.

Abstract

Over the last decades, semiconductor/noble metal multicomponent nanostructures have raised great interest owing to their promising potential in applying sustainable energy conversion, including solar-driven water splitting or photovoltaic components in solar cells.

In this thesis, I work on the wet-chemical synthesis of octahedral Cu_2O nanoparticles. Furthermore, I fabricate gold nanorod/octahedral Cu_2O core/shell and gold nanograin decorated octahedral Cu_2O heterostructured nanoparticles as two different multicomponent counterparts. Using these nanoparticle building blocks, I assemble monolithic cryoaerogels, opening a bridge between the nanoscopic and macroscopic world.

The structure and morphology of the nanoparticles are characterised by scanning and transmission electron microscopy, energy-dispersive X-ray spectroscopy, X-ray diffraction and total reflection X-ray fluorescence. I use different spectroscopic techniques to investigate their optical properties, including ultraviolet and visible spectroscopy, photoluminescence spectroscopy, and time-correlated single photon counting.

Table of contents

Introduction

The birth of nanotechnology dates back to the 20th century, with Richard P. Feynman's visionary lecture "There's Plenty of Room at the Bottom". Over the decades, nanoscience and nanotechnology became one of the most promising fields of the 21st century. It focuses on the fabrication, investigation and application of nanomaterials. Nanomaterials refer to the so-called nanoparticles, which have an extension between 1 – 100 nm at least in one dimension, as well as nanostructured materials. The latter are bulk materials with a microstructure that has characteristic length on the nanoscale. Due to the high surface to volume ratio, nanoparticles may possess new or different physical and chemical properties from those observed in the corresponding bulk material; such as reactivity, mechanical and optical properties, or biocompatibility. Thus, nanotechnology has attracted enormous attention in the last decades, which resulted in plenty of innovations, *e.g.* giant magnetoresistance, drug delivery systems, biomimetic, photonic, photovoltaic or metamaterials.[1,2]

For my diploma thesis, I worked on the synthesis of octahedral copper(I) oxide (Cu_2O) nanoparticles, as well as its two different heterostructures with gold. One type was a core-shell structured nanoparticle: I grew the octahedral Cu_2O on gold nanorods. In the other arrangement, I decorated the pristine Cu_2O nano octahedra with gold nanograins. I aimed to investigate how the Cu_2O nanoparticles' optical properties are affected by the presence of gold nanoparticles, as well as to investigate the impact of the gold's relative position within the system. This knowledge may help to design and implement catalytic properties more efficiently, which may be crucial in future applications. In the following chapter, I present the basic theoretical background for this work, and based on that I outline my detailed objectives.

1. Theoretical background

1.1. Heterostructured nanoparticles

In heterostructured inorganic nanoparticles (NPs), two or more components are connected through interfaces, with distinct composition, shape, or size on the nanoscale. These particles can integrate metals, semiconductors, insulators, plasmonic particles and other functional domains. The integrated, multicomponent structure do not only possess the properties of the pristine materials but owing to the synergy of the combined components, they may exhibit diverse functions, and improved or novel properties, which cannot be achieved by their physical mixture. These features enable their potential application in many areas, such as drug delivery, photonics, photovoltaics, or solar energy conversion including photocatalysis. Apart from the composition, heterostructured nanoparticles can be classified based on their geometrical configuration; *e.g.* core-shell, decorated or Janus-type structures. The impact of the geometrical arrangement can be particularly important in the case of plasmonic NPs since the plasmon resonance frequency can be finely modulated through the size, shape and environment of the particle. In noble metal – semiconductor heterostructured nanoparticles the plasmon-mediated energy transfer holds tremendous potential in solar-driven photocatalysis. For example, TiO_2 is one of the most widely studied photocatalytic materials, however, its main drawback is its wide bandgap which is problematic in solar-energy applications. By integrating plasmonic nanoparticles, this problem can be partly mitigated since their absorption is tuneable across the solar spectrum. Among the different kinds of nanomaterials, noble metal – metal oxide heterostructured nanoparticles have become an intensively studied area of research, thanks to their advantageous photocatalytic properties, such as CO_2 reduction, degradation of organic pollutants, and solar-driven photocatalytic water splitting. [3–5]

1.2. Optical properties of semiconductor nanoparticles

In principle, semiconductors are materials, whose electrical conductivity increases with increasing temperature, and its magnitude is between those of metals, such as gold or silver, and insulators like glasses. This property originates from its forbidden band, characterised by the E_g bandgap energy, which separates the last completely full band for electrons, the valance (*VB*), and the next higher energy band, the conduction bands (*CB*). In semiconductors, E_g usually ranges between $0.3 – 3.8$ eV. Semiconductor nanoparticles, whose size approaches the bottom of the nanoscale ($1 – 20$ nm) show remarkable optical and electronic properties. In this size range, most semiconductors show quantum confinement. For example, as the particle size decreases, the VB and CB split into discrete energy levels, and E_g increases as the particle size decreases. Through the strong size dependence of E_g, the particle's absorption and emission energy can be finely tuned across a wide spectral range, which gives rise to their application in bioimaging, solar energy conversion, quantum computing, and many other fields.[6] Although larger semiconductor NPs do not possess the extraordinary properties resulting from the quantum size effect, colloidal semiconductor particles have raised great interest owing to their promising potential in the application as photocatalytic material in water splitting or other chemical reactions, a photoactive component in solar cells, and so on mainly due to their well-defined and tuneable crystal facets.
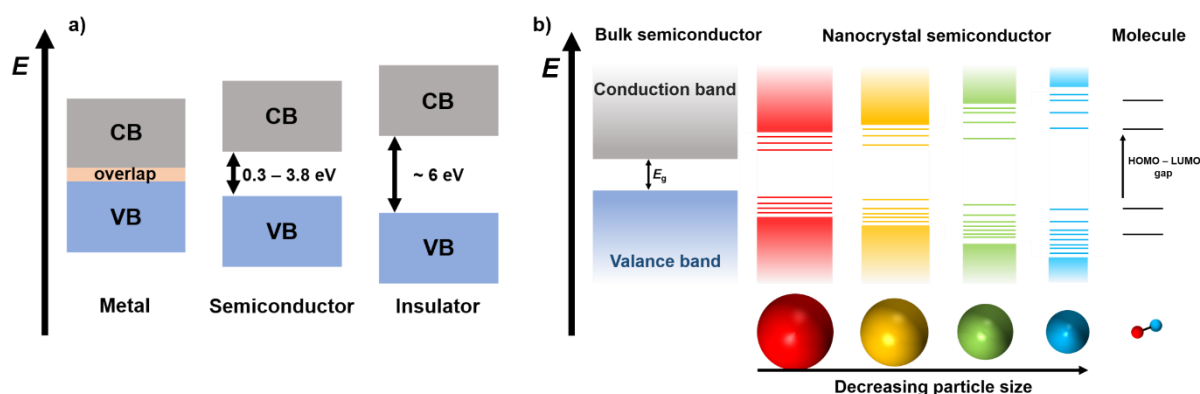
Figure 1. (a) Schematic illustration of the difference in the bandgap energy of a metal, semiconductor and insulator. (b) The band structure as well as the discrete energy levels in a bulk semiconductor, in nanocrystal semiconductors and in a molecule.

The large number of atoms in a bulk semiconductor (or colloidal particle) leads to the formation of a band structure. In any case, external energy (whether thermal, electronic or optical) can excite an electron (e⁻) from the VB to the CB. Under the irradiation of semiconductor material, absorption occurs only if the incident photon energy is greater than or equal to the E_g, below the adequate photon energy, the semiconductor is transparent. Consequently, E_g plays an

important role in determining the optical properties. The promotion of an e$^-$ to the CB leaves a positively charged hole (h$^+$) behind in the VB. These charge carriers may 'feel' each other's presence *via* Coulomb attraction and are correlated to some extent. This is referred to as an exciton. When the exciton binding energy (characteristic for the given material system) is provided, the exciton is separated into free charge carriers. The separated charges are free to move around in the VB and CB. The inverse process is called e$^-$ – h$^+$ recombination, when an e$^-$ decays from the CB to the VB, emitting a photon (radiative recombination, *i.e.* fluorescence) and/or generating phonons (non-radiative recombination). The lifetime of the radiative process by which electrons drop to the VB and E_g energy photons are emitted is in the order of nanoseconds. In the case of non-radiative recombination, the energy lost by the charge carriers is transferred to the lattice and finally released as heat. This process occurs *via* electron – phonon coupling, scattering, or indirectly *via* recombination centres such as the particle surface, grain boundaries, dislocations, vacancies, or any kind of impurities. The different recombination centres are located within the bandgap, where first, either an e$^-$ or a h$^+$ is captured, then subsequently the oppositely charged one. The charge carriers, captured by a defect, do not recombine immediately. It can be reemitted before capturing the oppositely charged one, in this case, the defect is called a trap, which can be shallow or deep depending on its energy. Besides the recombination, the charge carriers can diffuse to the particle surface, where they can reduce and/or oxidise compounds adsorbed on the particle surface. This is the basis of the application of semiconductor NPs as photocatalytic materials.
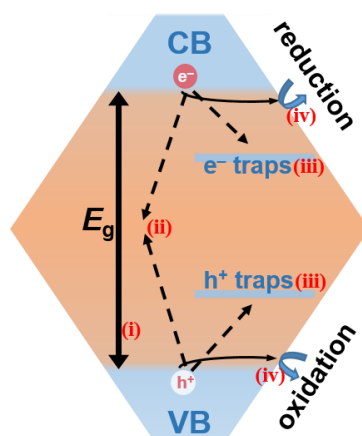
Figure 2. (i) Illustration of photon absorption/emission. The separated charge carriers can (ii) recombine in the particle, (iii) be trapped, or (iv) participate in surface reactions.

Metal oxide NPs are typical photocatalyst materials, due to the promising arrangement of electronic structure, light absorption properties and charge transport characteristics. Cuprous oxide (Cu$_2$O) is a p-type transition metal oxide semiconductor, with a bandgap of approximately 2.17 eV.[7] Its low-cost, abundant availability, nontoxicity and stability would make it a good

candidate for application as a photocatalytic material. However, the absorption range Cu_2O covers only a relatively small part of the solar spectrum, which limits the energy efficiency. This issue can be overcome by extending the absorption range to the visible and near-infrared range, *via* combining it with metals and integrating *e.g.* the plasmonic properties of a metal NP component.[8]

1.3. Optical properties of gold nanoparticles: localised surface plasmon resonance

Since ancient times, gold and other noble metal nanoparticle have been used – even if not intentionally – for many artistic objects, such as in the Lycurgus cup or some church windows, thanks to their bright colour when light falls on them.[9] The intense particle – light interaction originates from the so-called localised surface plasmon resonance (LSPR). According to the Drude model, the conduction band electrons can freely move within the particle, compared to the quasi-stationary metal ions in the lattice. A periodic external electromagnetic field (light) induces a coherent oscillation of these electrons (**Figure 3**), called plasmon in the literature. The plasmon frequency is the function of several particle parameters including its size, shape, and environment. If the frequency of the electromagnetic field matches the oscillation frequency of the conduction band electrons, the oscillation becomes resonant. This phenomenon is the so-called localised surface plasmon resonance.[10,11]
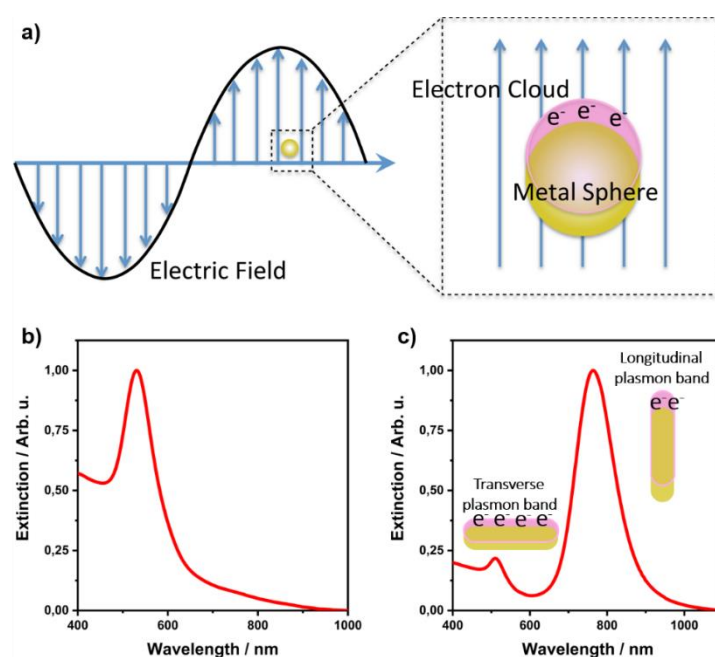

Figure 3. (a) Schematic illustration of the localised surface plasmon resonance in the case of gold nanospheres. (b) The typical extinction spectra of gold nanospheres and (c). nanorods.

During the particle – light interaction the radiation is partially absorbed (metals are inherently glossy) as well as scattering occurs. These two phenomena can be described with the absorption (σ_{abs}) and scattering (σ_{scat}) cross sections, the summation of which gives the extinction cross section (σ_{ext}). In the case of spherical particles:[12]

$$\sigma_{abs} = 4 \cdot \pi \cdot k \cdot r^3 \cdot \text{Im}\left[\frac{\varepsilon_p - \varepsilon_m}{\varepsilon_p + 2 \cdot \varepsilon_m}\right] \tag{1}$$

$$\sigma_{scat} = \frac{8}{3} \cdot \pi \cdot k^4 \cdot r^6 \cdot \text{Im}\left|\frac{\varepsilon_p - \varepsilon_m}{\varepsilon_p + 2 \cdot \varepsilon_m}\right|^2 \tag{2}$$

$$\sigma_{ext} = \sigma_{abs} + \sigma_{scat} \tag{3}$$

In the above equations, k is the wavenumber of the incident electromagnetic radiation, ε_m and ε_p are the dielectric constants of the media and the particle, respectively, r is the radius of the particle, and '*Im*' stands for the imaginary part. The equations show that the absorption is proportional to the volume of the particle, and the scattering is proportional to the volume square of the particle. Hence, the bigger the particle the more intense the specific scattering. Therefore, with increasing particle size the absorption's relative contribution to the extinction spectra becomes smaller and smaller, contrary to the contribution of the scattering, which becomes more and more dominant. This is illustrated in **Figure 4**. It shows three samples, containing different-sized spherical NPs in (a) transmitted and (b) reflected illumination. In the case of small particle size, the difference between the absorption and scattering is not significant. However, the sample with larger particles shows a remarkable difference.

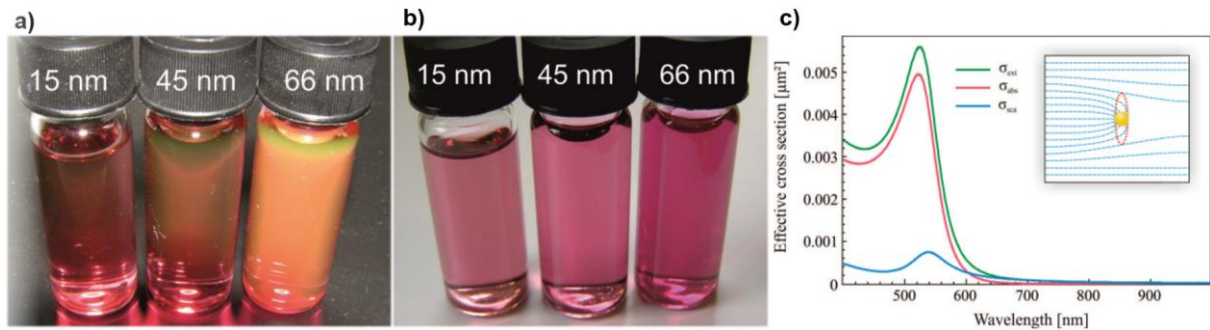**Figure 4.** Spherical gold NPs in (a) transmitted and (b) reflected illumination. (c) Effective cross section of a gold nanoparticle.[13,14]

The presence of an electromagnetic field induces the displacement of the conduction band electrons, which results in a charge distribution distortion within the particle. Due to the charge separation, electrostatic attraction takes place between the displaced electrons and the metal

ions. This electrostatic force attracts the electrons towards their equilibrium position, thereby, the polarization of the particle induces the coherent oscillation of the conduction band electrons. It can be described as a damped harmonic oscillator (dipole antenna). The model has three parameters; the spring constant (k), the effective mass of the electrons (m), and the damping (Γ). The plasmon frequency can be calculated according to equation 4:[15]

$$\omega = \sqrt{\frac{k}{m}} \tag{4}$$

The spring constant's magnitude is the function of particle shape, that is the particle geometry fundamentally affects the electron oscillation. In spherical particles, the electron oscillation is isometric due to the spherical symmetry. Therefore, its spectrum contains only one resonance peak (**Figure 3**. b). However, the particle shape may results in interesting differences. The simplest example of anisometric particle is the nanorod, which has the same extent in two dimensions of the space, and a larger extent in the third dimension. Consequently, the polarisation within the particle may take place in two different directions, thus both longitudinal and transverse modes exist (**Figure 3**. c).[16,17] As is demonstrated in **Figure 5**, the resonant frequency of nanorods does not depend on their size, but on their length-to-width ratio (aspect ratio). The longitudinal mode is particularly sensitive to the aspect ratio, thus the resonant frequency is finely tuneable.[18,19]
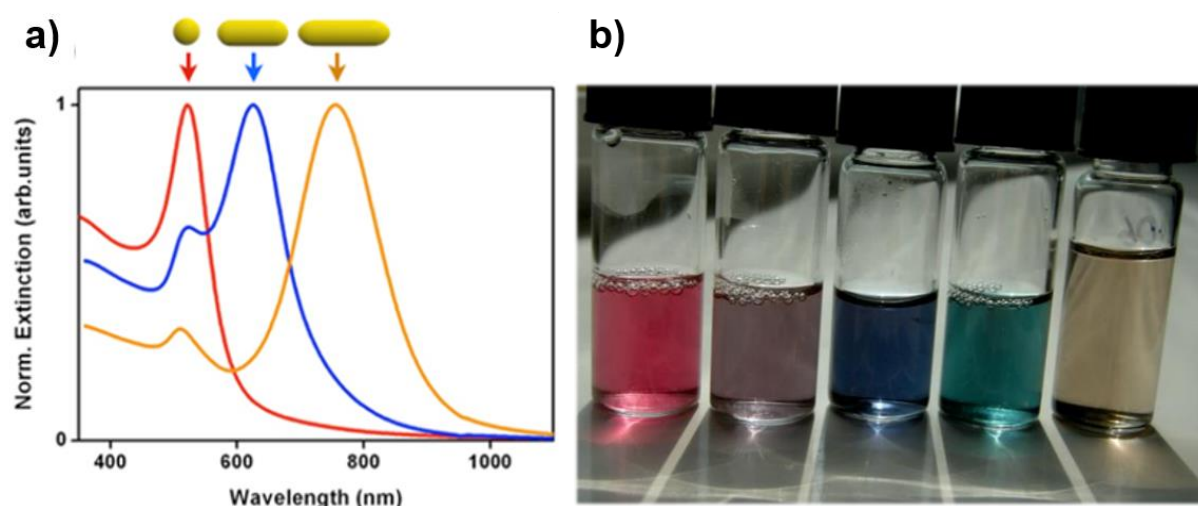

Figure 5. (a) Extinction spectra of a gold nanosphere as well as gold nanorods with different aspect ratios. (b) Gold nanorod solutions: the aspect ratio is increasing (from 1 to 4) from left to right.[14]

1.4. Noble metal – semiconductor heterostructured nanoparticles

In solar-driven photocatalysis, one of the main limiting factors of semiconductor NPs is their absorption range, which covers only a relatively small part of the solar spectrum. Utilising the LSPR, this limitation can be overcome. In semiconductors, charge separation in the plasmonic NP absorption range can be induced by the LSPR. Therefore, the absorption range of the semiconductor in heterostructured NPs can be extended from the UV up to the NIR region.

In heterostructured NPs, the interactions between the electronic states of the metal and the semiconductor lead to spectral shift and broadening in both the semiconductor's absorption peak and the plasmonic peak of the noble metal, *i.e.* the spectra of heterostructured NPs show a significant difference compared to the spectra of the physical mixture of the components.

At the metal – semiconductor interface some important phenomena arise from the electronic structure of the components. One is the formation of a Schottky junction, which leads to the migration of the charge carriers. In the case of a p-type semiconductor, it results in the accumulation of the positively charged holes on the metal and the negatively charged electrons on the semiconductor. Another effect is the Schottky barrier, which is the energy difference between the band edge of the semiconductor and the Fermi energy of the metal. It can promote the separation as well as prevent the recombination of the photogenerated charge carriers. As the separated electrons and holes can participate in reduction and oxidation reactions, respectively, these phenomena can improve the photocatalytic performance of the heterostructured NPs.[20]

Besides the impact on the charge carrier separation, noble metal NPs can also enhance the optical properties through the LSPR. In the literature, six mechanisms have been proposed to explain the synergetic interaction between the plasmonic metal and the semiconductor NPs:

  i.   Plasmon-induced hot electron transfer (PHET), or SPR sensitization
  ii. Plasmon-induced metal-to-semiconductor interfacial charge-transfer transition (PICTT), or direct electron transfer
  iii. Local electromagnetic field (LEMF) enhancement
  iv. Resonance energy transfer (RET)
  v.   Light scattering (LS) effect
  vi. Plasmonic heating (PH) effect.
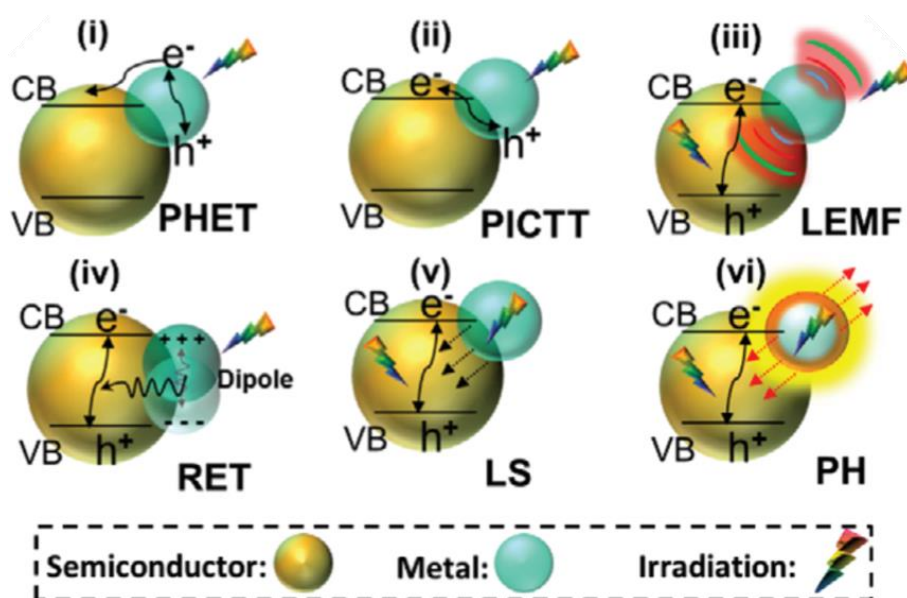
The above-listed mechanisms are depicted in **Figure 6**.

Figure 6. Schematic illustration of the different plasmon enhancement mechanisms in metal – semiconductor interactions.[5]

(*i*) After the LSPR excitation in plasmonic NPs, the electromagnetic decay can take place in either a radiative (*i.e.* scattering) or non-radiative (*i.e.* Landau damping) pathway. In the case of the non-radiative decay, the accumulated energy is transferred to electrons, generating so-called '*hot-electrons*'. If the plasmonic NP is in contact with a semiconductor, the hot-electrons with adequate energy can be injected into the CB of the neighbouring semiconductor. This process is the so-called plasmon-induced hot electron transfer. The required energy to surpass the Schottky barrier is significantly lower than the E_g semiconductor bandgap, and tunnelling, with a lower possibility is also possible. The efficiency of this process is limited by the thermalization of the hot electrons, as electron – electron and electron – phonon scattering takes place during the charge transfer.[21]
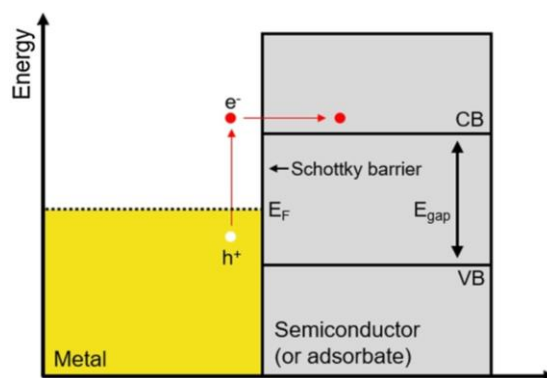

Figure 7. Schematic illustration of the plasmon-induced hot electron transfer mechanism. The hot electrons, generated as a result of the plasmon decay, can overcome the Schottky barrier and be injected into the semiconductor CB.[22]

(*ii*) Similar to PHET, the noble metal NP also serves as a light-collecting antenna in the plasmon-induced charge-transfer transition (PICTT). Here, however, the strong interdomain coupling of the components at the metal – semiconductor interface results in such a plasmon decay, where e⁻ and h⁺ are directly generated in the semiconductor's CB and the metal, respectively. This case is in contrast to PHET, since the hot electrons do not have to pass through the interface, the energy loss due to the charge carrier thermalization can be avoided.[23]
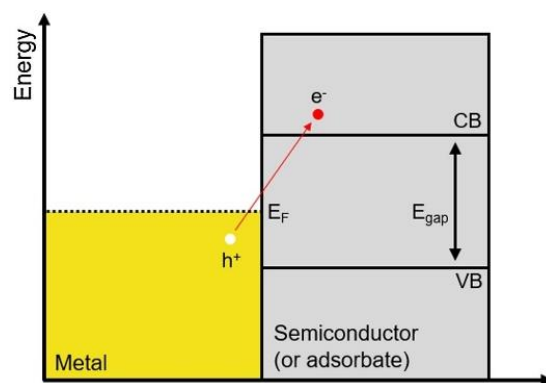
Figure 8. Schematic illustration of the plasmon-induced interfacial charge-transfer transition. The hot electrons are generated directly in the semiconductor CB, without the surpass of the Schottky barrier.[22]

(*iii*) In the case of the local electric field enhancement, the light-harvesting of the semiconductor is enhanced through the LSPR. Near to the surface of the plasmonic NP, the local electromagnetic field can be enhanced by several orders of magnitude because of the LSPR. This results in the amplification of the light absorption, e⁻ – h⁺ generation as well as the charge carrier separation in the semiconductor located in the vicinity of the plasmonic NP.[24]

Figure 9. Schematic illustration of the local electromagnetic field enhancement. By enhancing the local electromagnetic field, the 'plasmonic antenna' assists the e⁻ – h⁺ generation and separation in the semiconductor.[22]

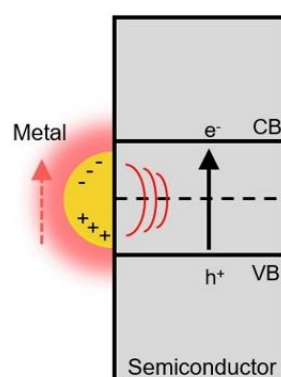(*iv*) Resonance energy transfer may arise if the semiconductor is located in the near field of the plasmonic NP, and the plasmon band spectrally overlap with the absorption band of the semiconductor. As previously discussed, in external electric field the oscillation of the conduction band electrons in the plasmonic NP results in an electric dipole, which oscillation frequency matches with the electric field of the incident light. Through dipole-dipole coupling between the plasmonic dipole moment and the $e^- - h^+$ pair dipole moment of the semiconductor, energy can transfer from the metal to the semiconductor. The energy transfer leads to $e^- - h^+$ pair excitation in the semiconductor.[24,25]
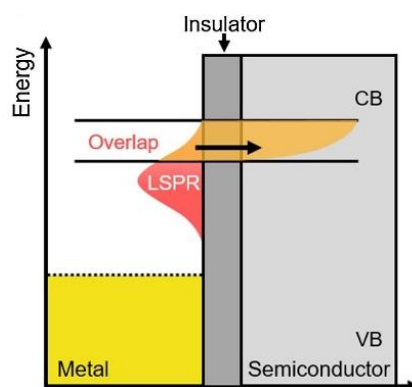
Figure 10. Schematic illustration of the resonance energy transfer. Through dipole-dipole interaction the excited plasmonic NP can transfer energy to the semiconductor, promoting $e^- - h^+$ pairs.[22]

(*v*) The light scattering effect of the plasmonic NP can significantly increase the number of incident photons that pass through the semiconductor. Through the radiative decay of the LSPR, an increased amount of photons can be directed towards the semiconductor to increase the possibility of the semiconductor – photon interaction, leading to the generation of more charge carriers.[26]

Figure 11. Schematic illustration of the light scattering effect. The intense light scattering of the plasmonic NPs increases the rate of the photons passing through the semiconductor.[22]

(*vi*) Plasmonic heating effect based on the photothermal effect. During non-radiative decay of LSPR, the plasmonic NP can release heat into the local environment. The rise in the temperature can drive chemical reactions as the reaction rate and the diffusion coefficient increase with the temperature.[22]

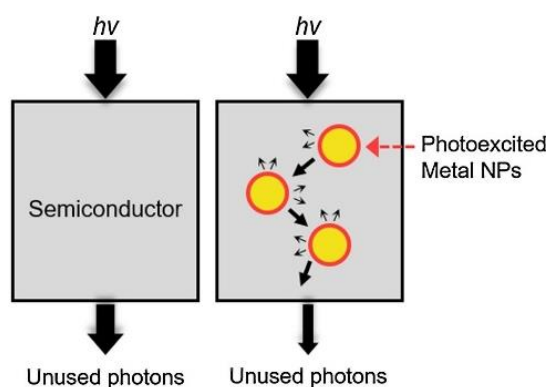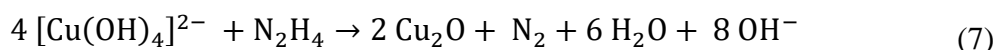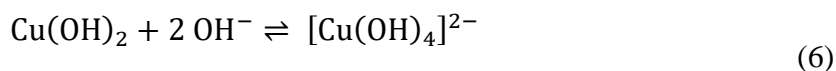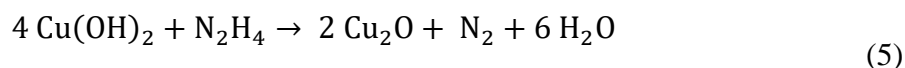The plasmonic NP can also influence the fluorescent properties of the semiconductor. As the LSPR results in a great enhancement of the local electromagnetic field, enhanced fluorescence can be achieved either through excitation enhancement, or emission enhancement. In excitation enhancement, the increased local electromagnetic field due to the metal NP increases the number of photoexcitation as well.[27] On the other hand, emission enhancement is based on the increased radiative decay rate. Since the enhanced electromagnetic field of the plasmonic NP is evanescent in nature, that is, it decays exponentially with the distance, accordingly, the distance between the plasmonic and semiconducting NPs should be optimized in the range of a few tens of nanometers.[28–30] Another aspect is the spectral overlap of the noble metal NP's plasmon band and the semiconductor NP's emission band: if the LSPR peak overlaps with the emission wavelength, the photoluminescence (PL) lifetime decreases, while the PL intensity increases.[31,32] If the semiconductor and noble metal NPs are in direct contact, in general, it results in fluorescence quenching, owing to the charge transfer from the excited semiconductor to the metal. This results in the spatial separation of the charge carriers if the Fermi level of the metal is located in the band gap of the semiconductor.

1.5. Nanoparticle synthesis

Nanoparticle synthesis can be categorised according to two strategies, the top-down and bottom-up approaches. In general, a top-down method is based on the disintegration of bulk material by physical or chemical processes (*e.g.* grinding, etching, and so on), whereas in the bottom-up synthesis the particles are constructed out of atoms and molecules; *via* wet-chemical techniques, physical or chemical vapour deposition, and so on. For example, in the 1850s Michael Faraday was the first who prepared colloidal gold solution using wet-chemical synthesis, which in fact, reserved its stability up to date. During wet-chemical approaches, by systematically modulating the reagents (reducing agent, surfactant, *etc.*) and the reaction conditions (temperature, stirring, *etc.*), desired size and shape can be achieved with narrow size distribution.

1.5.1. Synthesis of copper(I) oxide nano octahedra

The typical preparation procedure of Cu_2O NPs based on wet-chemical approaches, which provides the versatile ability to tailor particle size and shape, as well as high yields. Cu_2O NPs have been synthesised in various shapes, including spherical particles, nanowires, nanocubes, or octahedra. Among them, octahedral Cu_2O has attracted great attention due to their reactive {111} facets, which show high photocatalytic performance. The colloid solution can be prepared using a surfactant-free one-pot synthesis, in which copper nitrate ($Cu(NO_3)_2$), sodium hydroxide (NaOH) and hydrazine (N_2H_4) are involved. The reaction of the particle formation consists of two steps. First, the pH of a dilute aqueous $Cu^{2+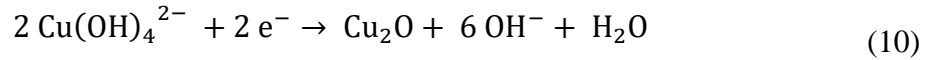}$ solution is adjusted with NaOH. The colourless solution turns blue, indicating the $Cu(OH)_2$ formation. In the second step, the particles are formed through the reduction of copper species by N_2H_4. A few seconds after N_2H_4 is introduced, the colour of the solution turns yellow-green and then gradually becomes orange, indicating the nucleation and the particle growth. The growth of the particles is also indicated by the solution becoming less transparent over time. The reaction can be described according to equations 5-7:[33,34]

$$4\,Cu(OH)_2 + N_2H_4 \rightarrow 2\,Cu_2O + N_2 + 6\,H_2O \tag{5}$$

$$Cu(OH)_2 + 2\,OH^- \rightleftharpoons [Cu(OH)_4]^{2-} \tag{6}$$

$$4\,[Cu(OH)_4]^{2-} + N_2H_4 \rightarrow 2\,Cu_2O + N_2 + 6\,H_2O + 8\,OH^- \tag{7}$$

Following the nucleation, the ratio (R) of the growth rate along $\langle 100 \rangle$ to that of the $\langle 111 \rangle$ zone axis determines the final shape of the particles. According to Wang, R = 1.73 leads to the formation of perfect octahedron bounded by only {111} facets (**Figure 12**. a.), whereas $0.87 < R < 1.73$ results in truncated octahedral particles bounded by {111} and {100} facets.[35] To this end, the volume of N_2H_4 should be precisely adjusted. The increasing amount of N_2H_4 increases the nucleation rate, resulting in various shaped particles, such as nanocubes, octapods or octahedra.[36] Besides the nucleation rate, N_2H_4, as a Lewis base, also influences the pH, which is also a factor in determining the shape-evolution of the particles. Thus, the NaOH concentration also has an impact on the particle shape: with increasing NaOH concentration, the growth habit of the particles transforms from cubic to octahedral (**Figure 12**. b.).[37] The effect of NaOH may be attributed to the increased oxidation potential of the $[Cu(OH)_4]^{2-}$ species with the increasing NaOH concentration, which can be deduced from the following equations:

$$Cu(OH)_2 + 2\,OH^- \rightleftharpoons [Cu(OH)_4]^{2-} \tag{8}$$

$$K = \frac{[Cu(OH)_4{}^{2-}]}{[OH^-]^2} \tag{9}$$

$$2\,Cu(OH)_4{}^{2-} + 2\,e^- \rightarrow Cu_2O + 6\,OH^- + H_2O \tag{10}$$
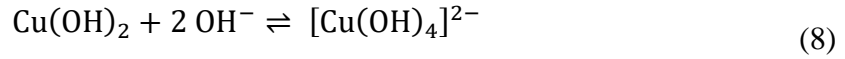
$$E = E^{\ominus} + \frac{0.0591}{2} lg \frac{[Cu(OH)_4{}^{2-}]^2}{[OH^-]^6} \tag{11}$$

$$E = E^{\ominus} + 0.0591 lg \frac{K}{[OH^-]} \tag{12}$$

Furthermore, the OH⁻ ions have different affinity to the crystal planes with different indices. The atomic arrangement of Cu and O atoms is different in the case of {111}, {110} or {100} facets (**Figure 12**. c.). For example, a perfect Cu_2O octahedron enclosed by {111} facets has coordination unsaturated Cu atoms at the surface, in which the Cu atoms have dangling bonds (**Figure 12**).[38] This results in different surface energy for the different facets, leading to different affinity with the OH⁻ ions, which can also influence the crystal growth process.

The as-prepared particle solution is centrifuged and the precipitate is dispersed in ethanol, which provides both the chemical as well as the colloidal stability.[39] Moreover, ethanol molecules have preferential adsorption on the {111} planes of Cu_2O, which provides the stability of the particles.[40]
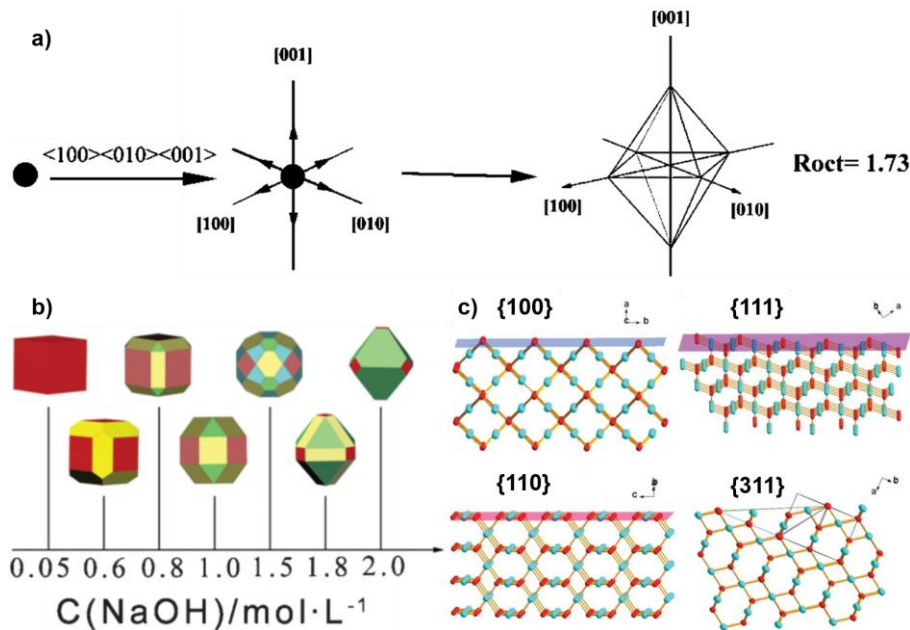

Figure 12. (a) Schematic illustration of the Cu_2O octahedral NP growth mode,[41] (b) the effect of the increasing NaOH concentration on the shape evolution, and (c) the surface structure of Cu_2O in the case of different crystal planes.[37]

1.5.2. Synthesis of gold nanorods

Nowadays, the most commonly used method in gold nanorod (AuNR) synthesis is the so-called seed-mediated approach. In this technique, the nucleation and growth of the NPs are separated. In the first step, the *seed solution* is prepared, which, in the second step, is injected into the *growth solution*, where the seed particles obtain their final anisometric shape and size. Separating the nucleation and growth phases provides a great control over the final shape and size of the particles. The main steps of the AuNR synthesis are illustrated in **Figure 13**:
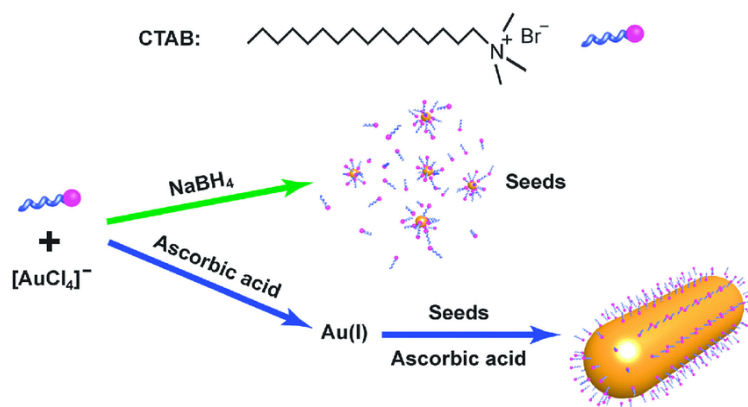

Figure 13. Schematic illustration of the seed-mediated gold nanorod synthesis.[42]

In an aqueous solution of hydrogen tetrachloroaurate (HAuCl$_4$) and cetyltrimethylammonium bromide (CTAB), the CTAB forms a complex with the Au^{3+} ions. The complex formation is indicated by the colour change of the solution: the yellow Au^{3+} solution turns into orange:

$$[AuCl_4]^- + 4\,CTAB \rightleftharpoons CTA^+[AuBr_4]^- + 4\,Cl^- + 3\,CTA^+ \tag{13}$$
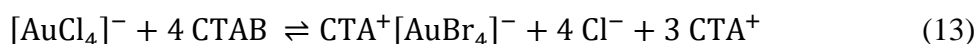
A strong reducing agent, *e.g.* sodium borohydride (NaBH$_4$) can reduce Au^{3+} into pristine Au^0, which leads to the formation of small (3 – 5 nm), spherical gold nanocrystals. These are the so-called seed particles. Gold nanorods are obtained by the further growth of the seed particles. The growth solution contains Au^{3+} ions, CTAB, ascorbic acid (AA), and several additives: sodium oleate (NaOL), silver nitrate (AgNO$_3$) and hydrochloric acid (HCl). Ascorbic acid is a weak reducing agent, it reduces the Au^{3+} ions into Au$^+$ ions:

$$CTA^+[AuBr_4]^- + C_6H_8O_6 \rightleftharpoons CTA^+[AuBr_2]^- + 2\,H^+ + +2\,Br^- \tag{14}$$

The further reduction of Au$^+$ takes place only after the addition of the seed, which catalyses the reduction owing to the high surface energy, leading to the growth of the particle. The particle surface is covered with CTA$^+$ which has a double role: it provides kinetic stability to the dispersion as well as acts as a template and influences the crystal growth mechanism. In principle, the seed crystals are not perfectly spherical, they have different sized and shaped

facets on their surface. To the different facets different surface energy is related, and the larger the surface energy the stronger the interaction between the crystal plane and the CTA^+. This facet dependent interaction may be the driving force of the anisotropic growth. The ratio of the seed particles and Au^{3+} ions has a significant influence on the particle size: with increasing the amount of seed particles, the nanorod width decreases, which means an increasing aspect ratio. Furthermore, the additives have also an enormous impact on the size and shape of the particles. For example, the nanorod length can be adjusted with the amount of Ag^+, the pH influences the geometry of the tips, and NaOL, which is one of the most promising additives, is promotes the formation of AuNRs with outstanding shape and size purity.[43]

1.5.3. Synthesis of copper(I) oxide – gold heterostructured nanoparticles

Noble metal – semiconductor heterostructured NPs are typically fabricated in two different arrangements. One is to deposit noble metal domains onto the surface of semiconductor NPs, referred to as decorated particles, and the other is the core – shell heterostructure, when the noble metal particle is embedded inside of the semiconductor particle (**Figure 14**). Both of them are of great interest due to their potential application as photocatalytic materials.
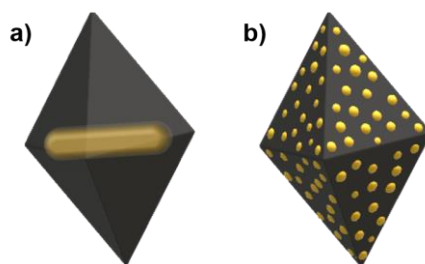
Figure 14. Schematic illustration of heterostructured NPs. (a) Core – shell structure: a gold nanorod is inside of a Cu_2O nano octahedron. (b) Decorated: gold nanograins are deposited on the outer surface of Cu_2O nano octahedron.

Similarly to the preparation process of AuNR synthesis, heterostructured nanoparticles can be fabricated *via* a seed-mediated approach. To a mixture, consists of AuNR seed particles, $Cu(NO_3)_2$, sodium dodecyl sulphate (SDS) and NaOH, a strong reducing agent (N_2H_4) is introduced, to induce the reduction of Cu_2O. Through heterogeneous nucleation, epitaxial growth of Cu_2O over the AuNRs results in core – shell heterostructured nanoparticles, in which a single AuNR is located at the centre of every Cu_2O octahedron. This process allows controlling the particle size by adjusting the amount of AuNRs and resulting in narrow size distribution and uniform shape.[44,45]

Gold nanograins can grow on the outer surface of Cu_2O nano octahedra through galvanic reaction, due to the standard potential difference between $AuCl_4^-$ / Au and Cu^{2+} / Cu_2O pairs. The process can be implemented by injecting $HAuCl_4$ solution into Cu_2O particle solution. The reduction of $AuCl_4^-$ ions by Cu_2O crystals is described by equation 15:[46]

$$3\,Cu_2O + 2\,AuCl_4^- + 6\,H^+ \rightarrow 6\,Cu^{2+} + 2\,Au + 3\,H_2O + 8\,Cl^- \qquad (15)$$
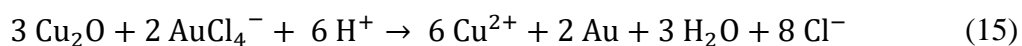
In principle, gold can be deposited selectively on the different parts of Cu_2O octahedra, exploiting the inhomogeneous distribution of surface energy (γ), following the order of $\gamma_{facets} < \gamma_{edges} < \gamma_{tips}$. Beyond a certain $AuCl_4^-$ concentration threshold, however, Au nanograins are grown on the surface homogeneously. Increasing further the amount of gold precursor leads to the etching of the Cu_2O particles, because of the galvanic reaction.[47–49]

1.6. Cryogelation

In general, cryoaerogels are highly porous network structures, in which the gel network is constructed from NP building blocks through interparticle connections, and the pores are filled with air. The formation of the gel structure based on the rapid freezing of the NP solution and its subsequent freeze-drying. **Figure 15.** schematically illustrates this process. A droplet of an aqueous NP solution is injected into liquid nitrogen, where the rapid freezing leads to the formation of small ice crystallites. The NP building blocks are excluded from the crystallites and assemble in the gaps between the ice crystallites. During freezing, the propagation of the crystallites' boundary presses the NPs together to form the sheet-like substructures of the self-supported network. Subsequently, the ice template is removed by freeze-drying, which process involves low pressure (below the triple point of water) in order to sublimate the water ice. This way the ice can be extracted avoiding the presence of the liquid phase, which, due to capillary forces, would lead to the collapse of the porous gel structure. Thus, a porous structure can be formed, where the ice crystals are replaced by air leading to an aerogel network of the nanoscopic building blocks. This novel assembly technique allows the fabrication of monolithic (self-supported) gel structures or cryogel coatings (via using a solid substrate as a support). One of the main advantages of this approach lies in its versatility: nanoparticles with diverse composition, surface chemistry and morphology can be gelated by means of this physical gelation method and the chemical modulation of the surface ligands is not needed.
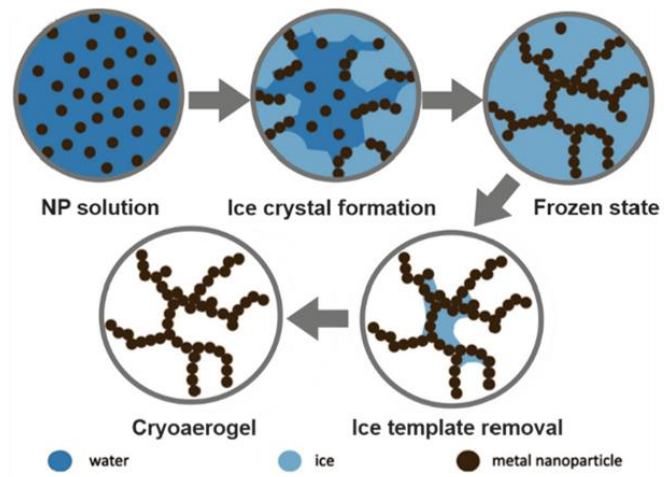
Figure 15. Schematic view of the freeze drying process.[50]

2. Detailed objectives

During my thesis work, my research focused on multicomponent nanoparticle systems built up from a semiconductor and a metal component. These nanoparticles are of great interest in the modern photocatalysis, where the photoexcited charge carriers emerging in the semiconductor can be spatially separated using a noble metal with an appropriate Fermi level. In this study, I aimed to fabricate octahedral Cu_2O NPs as well as its two different, multicomponent heterostructured counterparts containing gold as a noble metal. One of them is a core-shell type heterostructure, in which an octahedral Cu_2O shell is grown onto a gold nanorod core located in the centre of the particle. As its inverse counterpart, the outer surface of Cu_2O nano octahedron is decorated with gold nanograins. One of the main objectives is to synthesise these three different NP systems with the same particle morphology, furthermore, to obtain the same atomic ratio of gold and copper for the multicomponent NPs allowing them to be compared in terms of optical and structural properties. My further goal is to gain a deeper insight into the influence of the presence as well as the relative position of gold nanoparticles on the optical properties of the octahedral Cu_2O with special regard of extinction, absorption, photoluminescence, and the lifetime of the radiative charge carrier recombination. To take one step further towards the practical application of such multicomponent nanoparticle-based systems, I intend to fabricate macroscopic, monolithic, highly porous cryoaerogel structures from the NP building blocks.

3. Experimental section

3.1. Materials and instrumentation

3.1.1. Chemicals

- L-Ascorbic acid (BioXtra, ≥99,0%, Sigma-Aldrich)
- Cetyltrimethylammonium bromide (BioXtra, ≥99%, Sigma-Aldrich)
- Hydrochloric acid (≥37%, Sigma-Aldrich)
- Hydrogen tetrachloroaurate(III) trihydrate (trace metals basis, ≥99,9%, Sigma-Aldrich)
- Silver nitrate (trace metals basis, 99,9999%, Sigma-Aldrich)
- Sodium borohydride (ReagentPlus®, ≥99,0%, Sigma-Aldrich)
- Sodium oleate (≥99%, Sigma-Aldrich)
- Ultrapure water (Millipore, resistivity of 18.2 MΩ·cm @ 25 °C)

- Hydrazine monohydrate (99+%, Thermo Scientific, 64% N_2H_4 content)
- Sodium hydroxide (Reagent grade, Sigma-Aldrich)
- Sodium citrate tribasic dihydrate (ACS reagent, ≥99,0%, Sigma-Aldrich)
- Sodium dodecyl sulfate (ACS reagent, ≥99,0%, Sigma-Aldrich)
- Copper(II) chloride (powder, 99%, Sigma-Aldrich)
- Copper(II) nitrate trihydrate (puriss. p.a., Sigma-Aldrich)

3.1.2. Equipment

- Analytical balance (Ohaus corp., PA114C)
- Automatic pipettes (Eppendorf Research Plus)
- Centrifuge (Eppendorf 5804 Benchtop and MiniSpin plus, Eppendorf)
- Magnetic stirrer hotplate (IKA RCT Basic)
- Ultrasonic cleaner (Elma S10, Elmasonic)
- Water purification system (Millipore Elix 3, Millipore Simplicity 185)
- Energy dispersive X-ray spectrometer (Oxford Ultimax 40)

- Fibre coupled diode-array visible spectrometer (Thorlabs CCS200)
- Scanning electron microscope (Zeiss LEO1540 XB, field emission cathode)
- Spectrofluorometer (FS5, Edinburgh Instruments equipped with an integrating sphere and ultrafast TCSPC electronics)
- Transmission electron microscope (FEI THEMIS 200 Aberration Corrected TEM/STEM)
- UV-VIS-NIR spectrometer (Shimadzu UV-3600i Plus UV-Vis-NIR)
- XRD (Bruker AXS D8 Discover)
- TXRF (Lab-built custom device with silicon drift detector and Zr collimator)[51]

3.2. Synthesis procedures

During syntheses, I paid great attention to avoid any contamination. To this end, I used disposable tools (pipette tips, centrifuge tubes, plastic spatulas), or cleaned them (glasswares, stir bars) using freshly prepared *aqua regia*, rinsed with ultrapure water, and then dried them in a drying oven. The solutions I used were always freshly prepared, except for the gold(III) solution. The latter was freshly diluted from a pre-prepared, refrigerated 0.1 M stock solution. Analytical balance and automatic pipettes ensured the accurate measure and dispensing of the chemicals.

3.2.1. Synthesis of octahedral Cu_2O nanoparticles

The reproducible, high yield production of Cu_2O NPs with the desired shape, size, and narrow size distribution has been a major challenge. Although one can find several synthesis procedures in the literature, none of them was found to be reproducible. Thus, I performed a series of experiments, varying the conditions of the synthesis, the precursors and fine-tuning their amount, to synthesise highly monodisperse octahedral Cu_2O NPs with around 136 nm base edge length in a reproducible way.

The octahedral Cu_2O NPs were prepared as follows: copper nitrate ($Cu(NO_3)_2$) solution was added to water using a 250 mL glass bottle at room temperature with constant stirring. Sodium hydroxide (NaOH) was introduced under vigorous stirring. The colourless solution immediately turned blue, indicating the precipitation of $Cu(OH)_2$. Hydrazine (N_2H_4) was then injected into the solution, and vigorously stirred for a minute. The solution turned yellow-green after a few

seconds, and then gradually became orange, indicating the nucleation and growth of the Cu_2O NPs. The mixture was stirred slowly for 9 minutes, after which the particles were isolated *via* centrifugation at 5000 rcf for 10 minutes. The supernatant was removed, and the precipitate was dispersed in 10 mL ethanol and 10 mL water and centrifuged twice more to remove the unreacted reagents. Finally, the product was dispersed in 10 mL absolute ethanol (referred to as *ethanolic stock solution* in the following). This solution is stable and can be stored for months.

Table 1. The name and amount of chemicals I used for the octahedral Cu_2O NP synthesis.

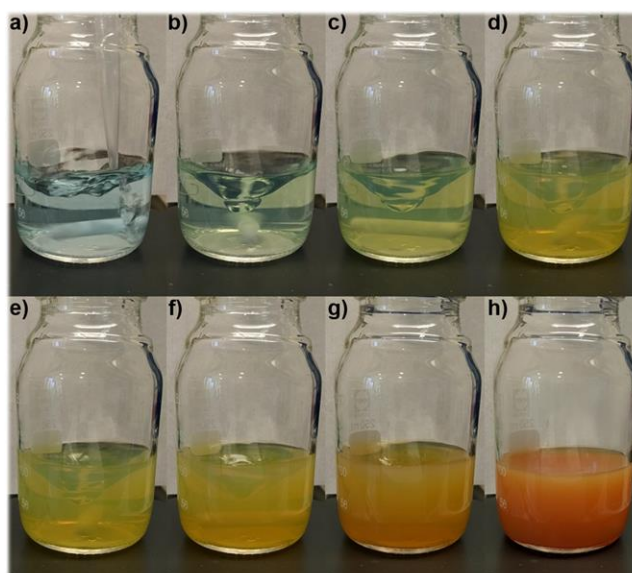| Chemical	Amount
H_2O	91.8 mL
$Cu(NO_3)_2$	1 mL (0.1 M)
NaOH	0.2 mL (1 M)
N_2H_4	3 mL (0.2 M)

Figure 16. Synthesis of octahedral Cu_2O NPs. (a) Before the addition of N_2H_4. (b) – (c) After the addition of N_2H_4. (h) The final product.

3.2.2. Synthesis of gold nanorods

I aimed to synthesise gold nanorods with dimensions around (30×90) nm, with narrow size distribution using a slightly modified version of a procedure reported by Ye *et al.*[43] The procedure consists of two steps. First, I simultaneously prepared the so-called growth and seed solutions. In the second step, I injected a certain amount of seed into the growth solution. **Table 2.** contains the chemicals and their amounts I used in this synthesis.

To prepare the growth solution (**Figure 17**. a), the cetyltrimethylammonium bromide (CTAB) and the sodium oleate (NaOL) were dissolved in 25 mL water using a glass bottle at the temperature of 50 °C with constant stirring. After the complete dissolution, the solution was allowed to cool down to 30 °C and silver nitrate ($AgNO_3$) was added to the mixture. The solution was left undisturbed for 15 minutes, after which the hydrogen tetrachloroaurate ($HAuCl_4$) solution was added and stirred slowly for 90 minutes. During this time the yellow solution became colourless, indicating the slow reduction of Au^{3+} to Au^+. The pH was adjusted to around 1.4 with the addition of concentrated hydrochloric acid (HCl). After 15 minutes, ascorbic acid (AA) was introduced with vigorous stirring, which was followed by the injection of the seed solution after 30 seconds. The mixture was left undisturbed overnight in a 28 °C bath, then centrifuged at 8000 rcf for 20 minutes. The supernatant was removed, and the precipitate was redispersed in 25 mL 50 mM CTAB solution.

Table 2. The name and amount of chemicals I used for the AuNR synthesis.

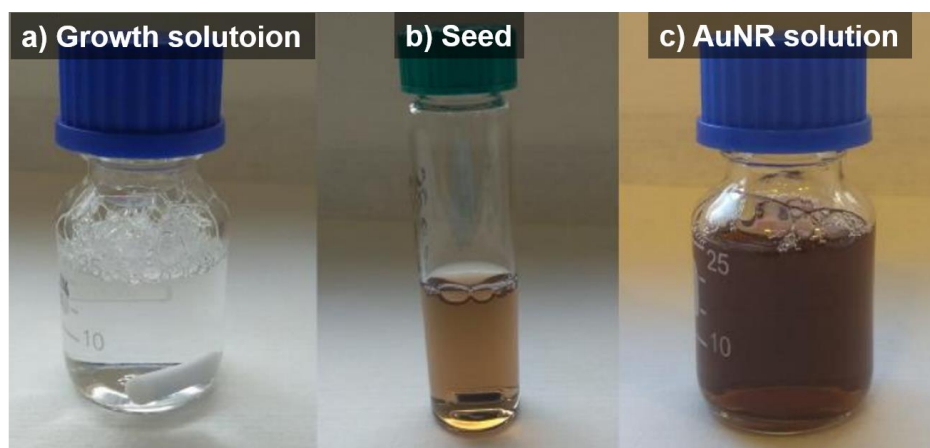|	Chemical	Amount
Growth solution	CTAB	0.9 g
	NaOL	0.1543g
	$AgNO_3$	1.8 mL (4 mM)
	$HAuCl_4$	25 mL (1 mM)
	HCl	0.21 mL (≥37%)
	AA	0.125 mL (0.064 M)
Seed	CTAB	5 mL (0.5 mM)
	$HAuCl_4$	5 mL (0.2 M)
	$NaBH_4$	1 mL (6 mM)

Figure 17. The images I made during the gold nanorod synthesis.
(a) The growth solution, (b) the seed, and (c) the AuNR solution.

3.2.3. Synthesis of AuNR@Cu$_2$O multicomponent nanoparticles

I synthesised gold nanorod/octahedral Cu$_2$O core/shell heterostructured NPs (referred as *AuNR@Cu$_2$O* in the following) with the same dimensions as the previously synthesised pristine Cu$_2$O nano octahedra, using a slightly modified version of a procedure reported by Kong *et al*.[44] To fabricate AuNR@Cu$_2$O, I used the previously synthesised gold nanorods, which, as seed particles, acted as the nucleation centres for the Cu$_2$O shell.

First, in order to set the proper particle concentration for the further steps of the synthesis, I concentrated the as-prepared AuNR solution. To this end, I centrifuged 31.053 mL AuNR solution at 3000 rcf for 20 minutes, removed the supernatant and redispersed the precipitant in 18 mL water. This ends up with a $c^{Au(0)} = 0.6257$ mM AuNR solution. To reduce the CTAB concentration an additional washing step was performed. **Table 3.** contains the chemicals I used in the synthesis.

The octahedral Cu$_2$O was grown around the AuNR seed particles at room temperature as follows: Cu(NO$_3$)$_2$·3 H$_2$O and sodium dodecyl sulphate (SDS) were dissolved in 25 mL water using a 100 mL glass bottle at room temperature with constant stirring. AuNR solution was introduced to the solution, and then NaOH was added under vigorous stirring. After 15 minutes, N$_2$H$_4$ was added dropwise (1 droplet/s) over 3 minutes, and the mixture was kept gently stirred. After 40 minutes, the product was centrifuged at 5000 rcf for 10 minutes. The supernatant was removed, and the precipitate was redispersed in 10 mL ethanol and 10 mL water, and centrifuged twice more. Finally, the product was redispersed in 5 mL absolute ethanol to achieve an ethanolic stock solution.

Table 3. The name and amount of chemicals I used for the synthesis of AuNR@Cu$_2$O.

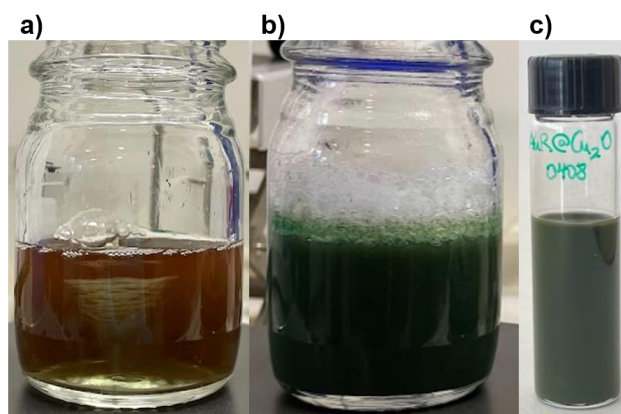| Chemical	Amount
Cu(NO$_3$)$_2$·3 H$_2$O	0.0755 g
SDS	0.9013 g
AuNR solution	17.5 mL $c^{Au(0)}$=0.6257mM
NaOH	6.25 mL (2 M)
N$_2$H$_4$	6.375 mL (0.4 M)

Figure 18. Synthesis of AuNR@Cu$_2$O. (a) Before and (b) after the addition of N$_2$H$_4$. (c) The final product after concentration and purification.

3.2.4. Synthesis of Cu$_2$O@Au multicomponent nanoparticles

I synthesised gold nanograin-decorated octahedral Cu$_2$O nano nanoparticles (referred as *Cu$_2$O@Au* in the following) using the previously synthesised pristine Cu$_2$O nano octahedra, serving as the nucleation centres for the Au nanograins. The Au nanograins were grown onto the octahedral Cu$_2$O NPs at room temperature as follows: 2.5 mL as-synthesised ethanolic Cu$_2$O NP solution was centrifuged at 5600 rcf for 10 minutes. The supernatant was removed, and the precipitate was redispersed in 25 mL water using a 100 mL glass bottle. Under vigorous stirring 25 mL of 0.0116 mM HAuCl$_4$ solution was then quickly poured from a flask into the solution. After 1 minute, the stirring bar was removed, and the mixture was left undisturbed. After 19 minutes the product was centrifuged at 5000 rcf for 10 minutes. The supernatant was removed and the precipitate was redispersed in 5 mL absolute ethanol to obtain the ethanolic stock solution.

Figure 19. Synthesis of Cu$_2$O@Au. The as synthesised heterostructured NPs (a) before and (b) after the purification.

3.3. Characterisation techniques

3.3.1. Ultraviolet and visible (UV-VIS) spectrophotometry

UV-VIS spectroscopy is a convenient technique used to study the optical properties of NPs. The extinction spectra of gold NPs were measured with a conventional fibre coupled diode-array spectrometer (

Figure 20. a.), operating in the visible range. The measurements of Cu_2O and heterostructured NPs were carried out using a double beam UV-VIS spectrophotometer (

Figure 20. b.), which enables extending the range of the measurement into the ultraviolet range. The measurement is based on the decrease in intensity of the irradiated light as a function of wavelength. To this end, the *I* intensity of light passing through the sample is compared to the I_0 intensity of light passing through the reference (*i.e.* dispersion medium). The ratio I/I_0 gives the transmittance (*T*), from which the absorbance (*A*) of the sample is expressed as:

$$A = -log_{10}\left(\frac{I}{I_0}\right) = -log_{10}(T) \tag{16}$$

I measured the extinction spectra of gold NPs using disposable plastic cuvettes with an optical length of 10 mm, to avoid cross-contamination. For the measurement of Cu_2O and heterostructured NPs, I used quartz cuvettes with the same geometry, which allows the measurement into the UV region. The shape, wavelength maxima and shifts in peak positions of the spectra provide qualitative information about the particles; including the size, size distribution, geometry, morphology, and stability. Through measuring the spectra of the samples, I was able to monitor the synthesis processes as well as the stability of the synthesised particles.

Figure 20. (a) Fibre coupled diode-array spectrometer and (b) UV-VIS spectrophotometer.

3.3.2. Photoluminescence spectroscopy (PL)

Photoluminescence spectroscopy is an important technique to characterise the optical response of semiconductor NPs upon illumination. The intensity and wavelength of the photons emitted from the sample under excitation provide information about the electron transition energies. The PL intensity is proportional to the recombination rate of the photogenerated $e^- - h^+$ pairs. The wavelength corresponds to the optical processes involved in the recombination. In steady state PL measurements, a Xe lamp serves as the excitation source, and there are two basic operation modes: the excitation and emission scans. The excitation spectrum is recorded, when the fluorescence intensity is measured at a certain (fixed) emission wavelength, as a function of the excitation wavelength. On the other hand, the fluorescence intensity can be recorded as a function of the emission wavelength, along with a monochromatic excitation at a fixed excitation wavelength, resulting in the emission spectrum. In time resolved photoluminescence (TRPL or TCSPC refers to time-correlated single photon counting) the PL decay is measured, that is the lifetime of the radiative recombination of the charge carriers. To this end, a pulsed diode laser is used for the excitation, which irradiates the sample with sub-nanosecond pulses with a certain repetition rate that allows to measure the tail of the decay. Investigating the PL decay provides information about the radiative exciton recombination and different defects in the crystal lattice, which are able to trap the charge carriers, inhibiting the band-edge recombination and serving as relaxation pathways.
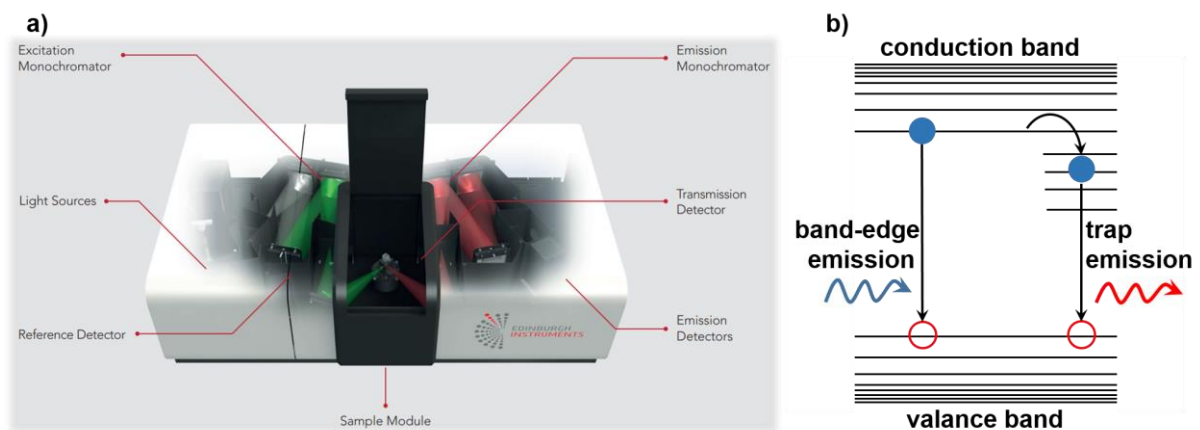

Figure 21. (a) Schematic drawing of a spectrofluorometer and its main parts. (b) Representation of band-edge and trap emissions.

3.3.3. Scanning electron microscopy (SEM)

Scanning electron microscopy is an important technique in the characterisation of particle size and morphology, producing images of the surface of the sample. The principles of SEM operation are based on the interaction between high-energy electrons and atoms in the sample. During the measurement, a focussed electron beam scans the sample surface from point to point, causing a series of phenomena at different penetration depths. This results in the production of different particles including backscattered and secondary electrons, as well as characteristic X-ray photons (**Figure 22. b.**) The secondary electrons are the main source of the imaging: their intensity is measured and converted into electrical signals, which modulate the brightness of the pixels on the screen. During the scanning, as the intensity of the secondary electron emission is changing from point to point, the brightness of the screen changes from pixel to pixel, drawing an intensity map (*i.e.* the microscopic image) of the sample surface. **Figure 22** displays a schematic view of the SEM. The magnification of the microscope is primarily determined by the size of the area in which the electron beam is focussed: the smaller the are the higher the achievable magnification.
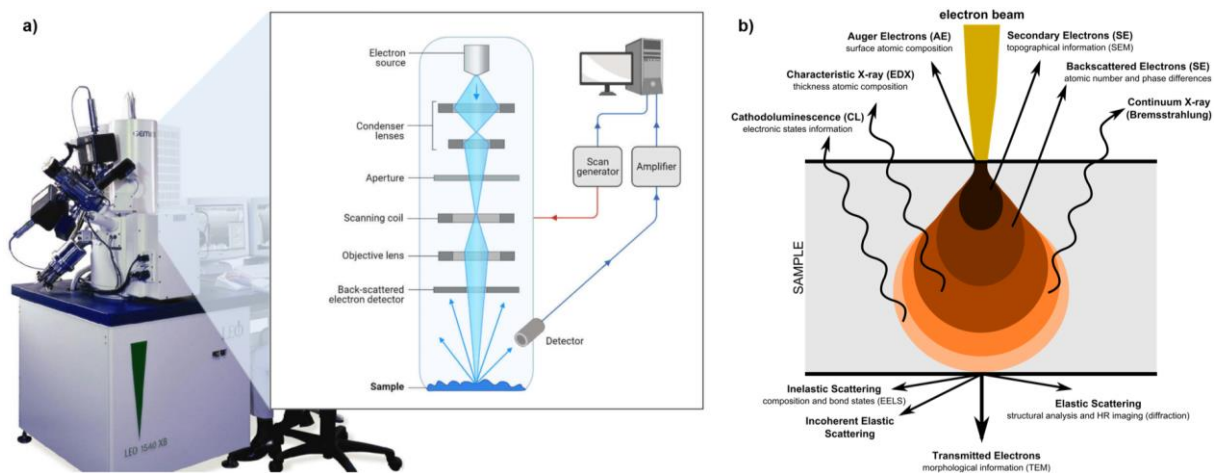

Figure 22.[52] (a) The electron source is a field emission cathode, from which electrons are emitted, accelerated by a positive voltage bias, focussed by the condenser lenses, which are then driven to scan the sample by the scanning coil. The particles originate from the electron beam – sample interaction are collected by dedicated detectors, which signal is converted into the image. (b) Different products from the electron – sample interaction, as a function of depth. Secondary electrons originate from the top 50 nm, backscattered electrons originate from the top 1-2 μm and X-ray photons originate from the top 1 - 2 μm layer of the sample.

3.3.4. Transmission electron microscopy (TEM)

Transmission electron microscopy is an important technique both in imaging as well as in analysing the crystal structure of the sample. Similarly to SEM, the operation of TEM is based on the interaction between the electron beam and the sample. In the case of TEM, the electron beam crosses the specimen resulting in forward scattered, elastically scattered and inelastically scattered electrons, which are detected to form the microscopic image or the diffraction pattern (**Figure 23**. b.). In imaging mode, the operation of TEM is analogous to that of the conventional optical microscopes, except electromagnetic coils are used to focus the electron beam by controlling the current. An objective aperture in the back focal plane allows only the direct or only diffracted beams to pass through, resulting in the bright field or dark field images, respectively. In the case of diffraction mode, the diffraction pattern consists of dots in the case of single crystals, or concentric rings in the case of polycrystalline and amorphous materials. **Figure 23. a.** displays a schematic view of TEM.
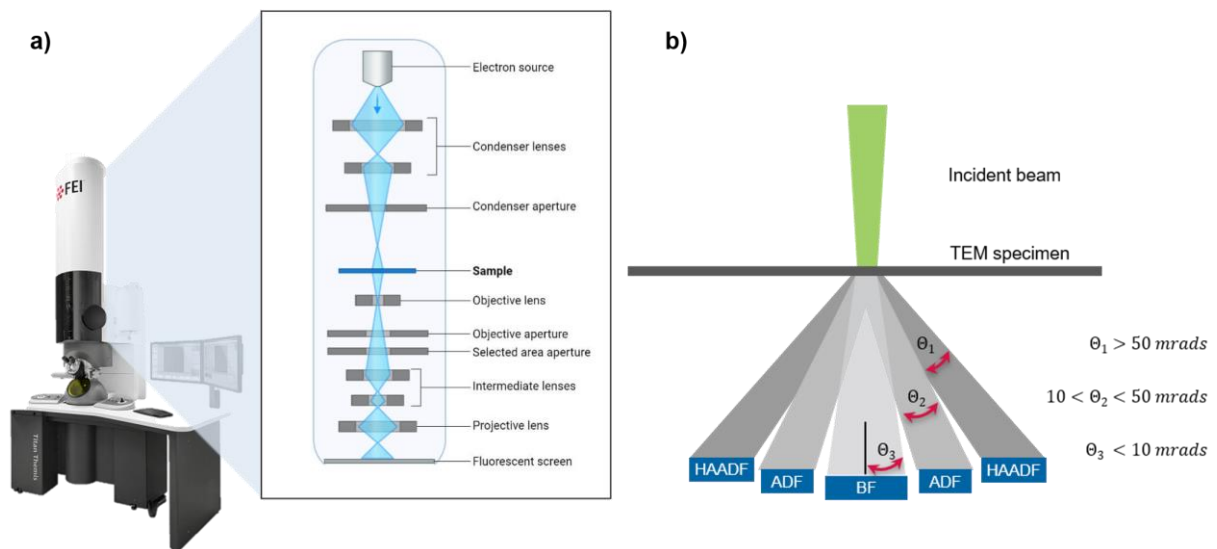

Figure 23.[52] (a) Schematic illustration of a TEM and (b) the electron beam – sample interaction.

3.3.5. Energy-dispersive X-ray spectroscopy (EDS)

Electron microscopic instruments, such as SEM and TEM are usually coupled with an energy dispersive X-ray spectrometer. Resulting from the electron beam – sample interaction characteristic X-ray photons are produced, which enables to analyse the elemental composition of the surface of the sample. The high energy electron beam can ionise the atoms of the sample

resulting in the emission of an inner shell electron. When the produced hole is filled by a higher energy level electron, the excess energy is emitted in the form of a characteristic X-ray photon.
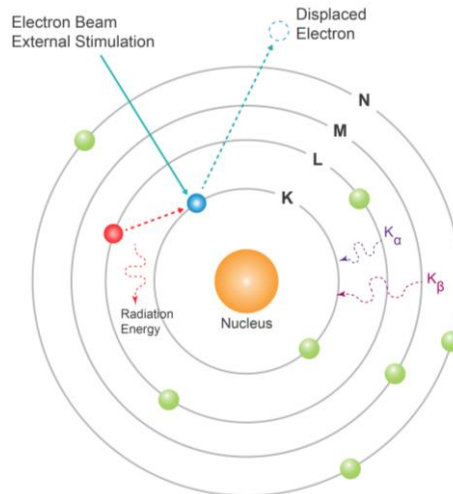

Figure 24. Due to external stimuli, an inner shell (K) electron is ejected leaving behind a hole. Subsequently, an electron from a higher energy level (L or M) fills the hole, releasing the excess energy (K_α or K_β, respectively) in the form of an X-ray photon emission.

3.3.6. Total reflection X-ray fluorescence (TXRF)

The total reflection X-ray fluorescence analysis provides both qualitative and quantitative information about the sample. The basis of the measurement is the detection of characteristic photons emitted by atoms of the sample under X-ray irradiation. Incident X-ray can ionise the atoms of the sample resulting in the emission of an inner shell electron. An outer shell electron can fill the hole, releasing the excess energy by the emission of an X-ray, which is characteristic for the element. In TXRF, the sample is irradiated with a totally reflected beam, reducing the absorption and scattering by the sample (*i.e.* the matrix effect), which results in enhanced fluorescence yield, a better signal-to-noise ratio and higher sensitivity. The intensity of a certain characteristic X-ray provides quantitative information of that particular element in the sample. With the addition of an internal standard, which is a single element standard with known concentration that is not present in the sample, gives the concentration of all the other elements that is present in the sample.
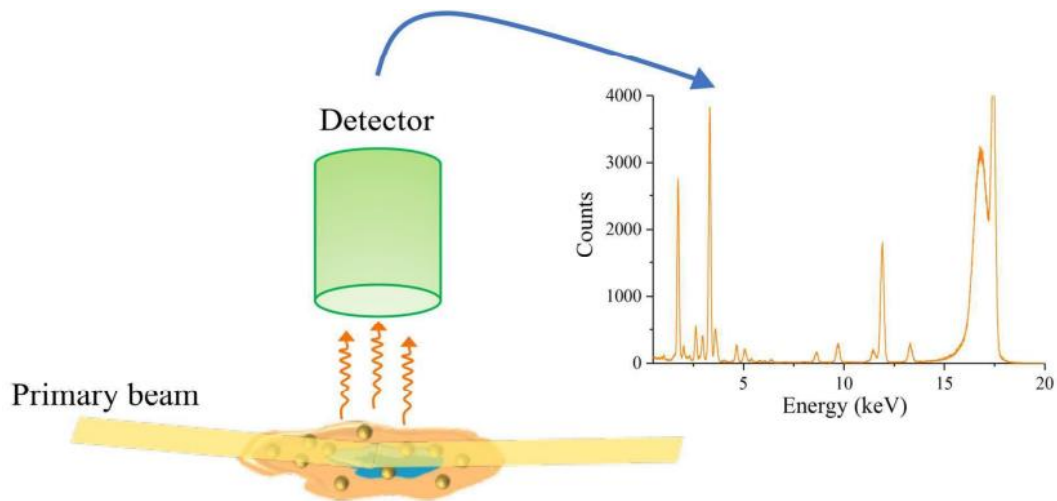
Figure 25. A schematic view of the total reflection X-ray fluorescence analysis.[53]

3.3.7. X-ray diffraction spectroscopy (XRD)

X-ray diffraction is a technique that can be used for phase identification of crystalline materials, it provides information about the atomic arrangement and crystal structure of the sample. XRD is based on the interference of monochromatic X-rays and atoms configured in regular arrays in the lattice. Constructive interference arises when the conditions satisfy Bragg's law:

$$n \cdot \lambda = 2 \cdot d \cdot \sin\theta \qquad (17)$$

where *n* integer is the diffraction order, λ is the wavelength of the incident X-rays, *d* is the distance of the crystal planes and Θ Bragg angle is the angle between the incident X-rays and the scattering planes as illustrated in *Figure 26*. Every crystalline material has a unique diffraction pattern, like a "fingerprint", that is characteristic to the particular crystal phase. A certain structure can be identified by comparing the measured pattern with a standard reference.
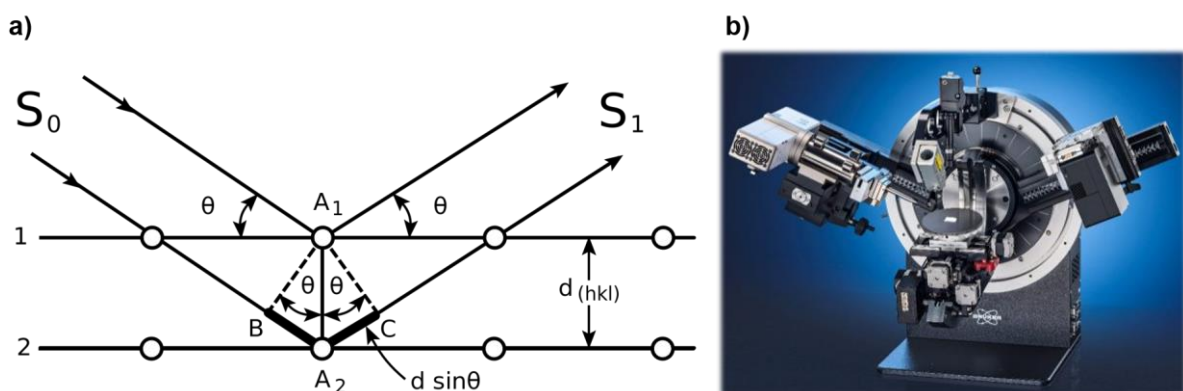

Figure 26. (a) Scheme of the Bragg diffraction. Constructive interference arises upon the incident X-rays fulfil Bragg's law. (b) An X-ray diffractometer.

4. Results and discussion

4.1. Morphological and size control of nanoparticle building blocks

4.1.1. Synthesis of pristine Cu₂O nano octahedrons

In order to obtain pristine Cu_2O nanoparticles with octahedral shape and within the desired size range, I attempted to reproduce several procedures from the literature. Ke *et al.* reported a series of synthesis using $NaOH$, N_2H_4 and $Cu(NO_3)_2$ to produce octahedral Cu_2O NPs with tunable edge lengths between ca. 50 – 150 nm by adjusting the amount of $NaOH$.[34]
My reproduction of the synthesis resulted in octahedral NPs with the desired shape, but the size distribution was enormously large for all samples. I have attempted to purify the samples *via* separating the larger particles with centrifugation, but I have not succeeded. The as-prepared particle solutions, as well as the extinction spectra and the related SEM images of one of the samples are shown below:
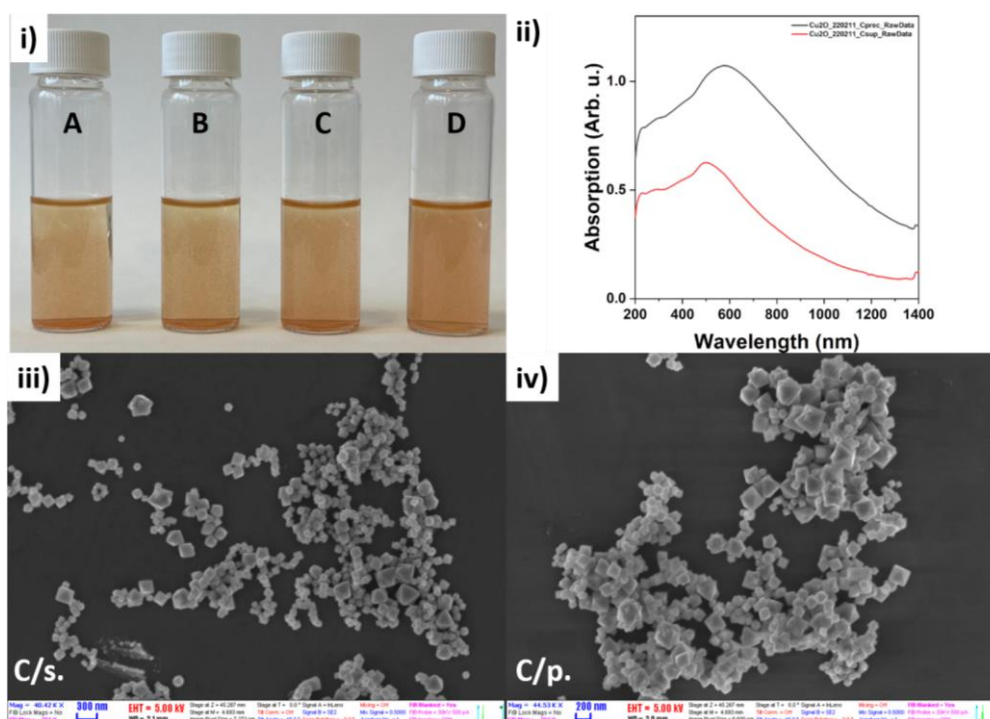

Figure 27. (*i*) The as-synthesised Cu_2O NPs, (*ii*) the extinction spectra of the supernatant (red) and precipitate (black) of *sample C*, and SEM images of the (*iii*) supernatant and the (*iv*) precipitate of *sample C*. The extinction spectra and representative SEM images of *samples A*, *B* and *D* are in the appendices (Figure 1. Ap.).

Saada *et al.* reported a procedure synthesising octahedral Cu_2O NPs using copper (II) chloride ($CuCl_2$), hydroxylamine hydrochloride ($NH_2OH \cdot HCl$), SDS and NaOH.[54]

To reproduce the synthesis, I performed 6 parallel experiments simultaneously, under the same conditions, using the same precursors in the same quantities. In principle, the 6 samples should have been identical. In contrary, the colours of the as synthesised samples were different, as well as their extinction spectra. Only one of them (*sample II*) showed the characteristic spectrum of the octahedral Cu_2O NPs, even though its extinction peak was quite broad, indicating the polydispersity of the sample. The SEM measurements confirmed that the 6 samples were significantly different, and besides the octahedral NPs, they contained octapods, nanospheres, and amorphous particles. In addition, their surface was not smooth. The polydispersity of *sample II* is also confirmed by the SEM images. The as-prepared particle solutions, the extinction spectra and the SEM images are shown below:
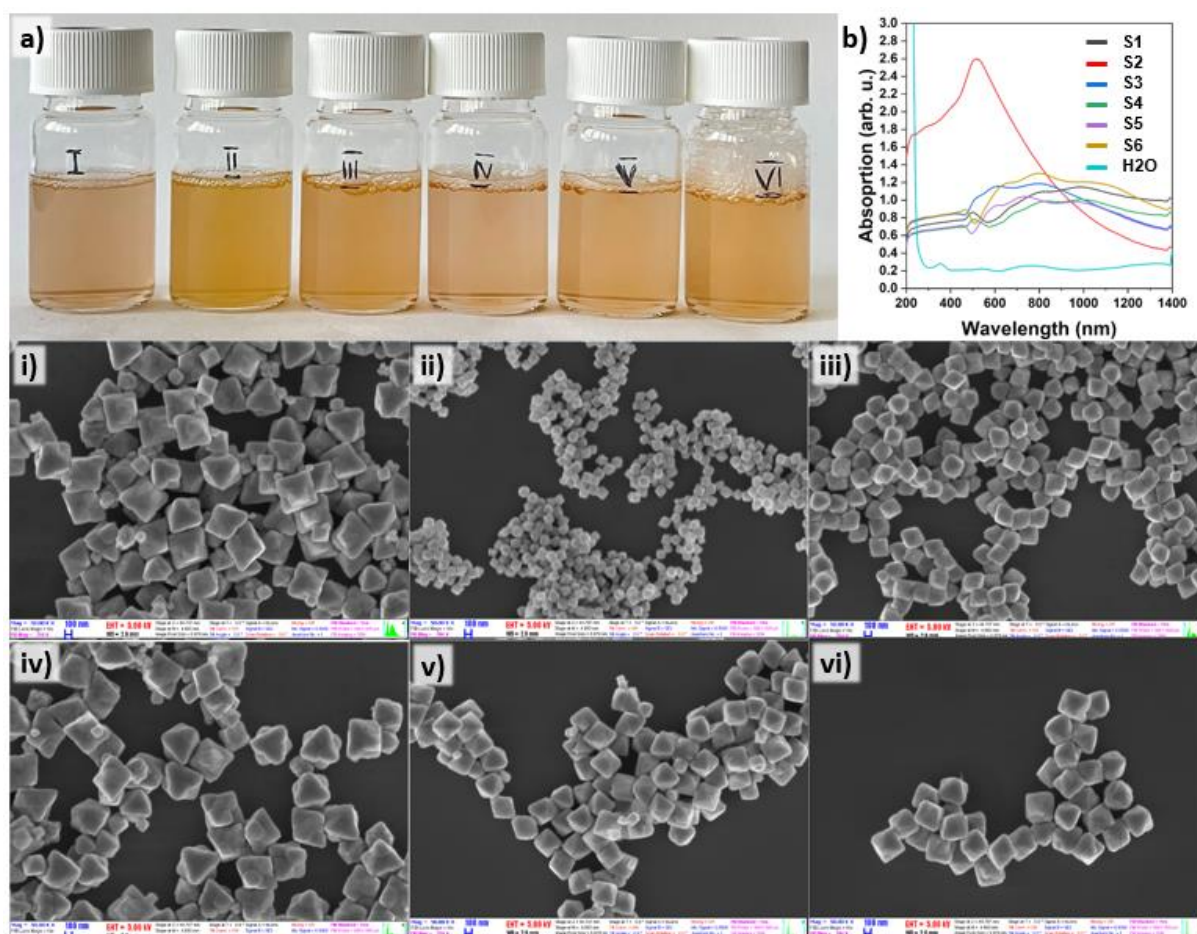

Figure 28. (a) The as synthesised particles, (b) the extinction spectra of the 6 samples and (i) – (iv) the related representative SEM images.

Pastrián *et al.*[55] reported another procedure similar to that of Saada *et al.*, using the same precursors: $CuCl_2$, $NH_2OH \cdot HCl$, SDS and NaOH. The reproduction of this synthesis route led to identical colour of the as-prepared solutions, and their extinction spectra were similar as well. However, the spectra did not show the characteristics of octahedral Cu_2O NPs. The wide spectral peaks indicated large polydispersity (as well as large average size) of the samples. The SEM images confirmed that the shape of the particles was barely octahedral, the samples contained many octapods and merged particles, and the samples were highly polydisperse. The as-prepared particle solutions, the extinction spectra and the SEM images are shown below:
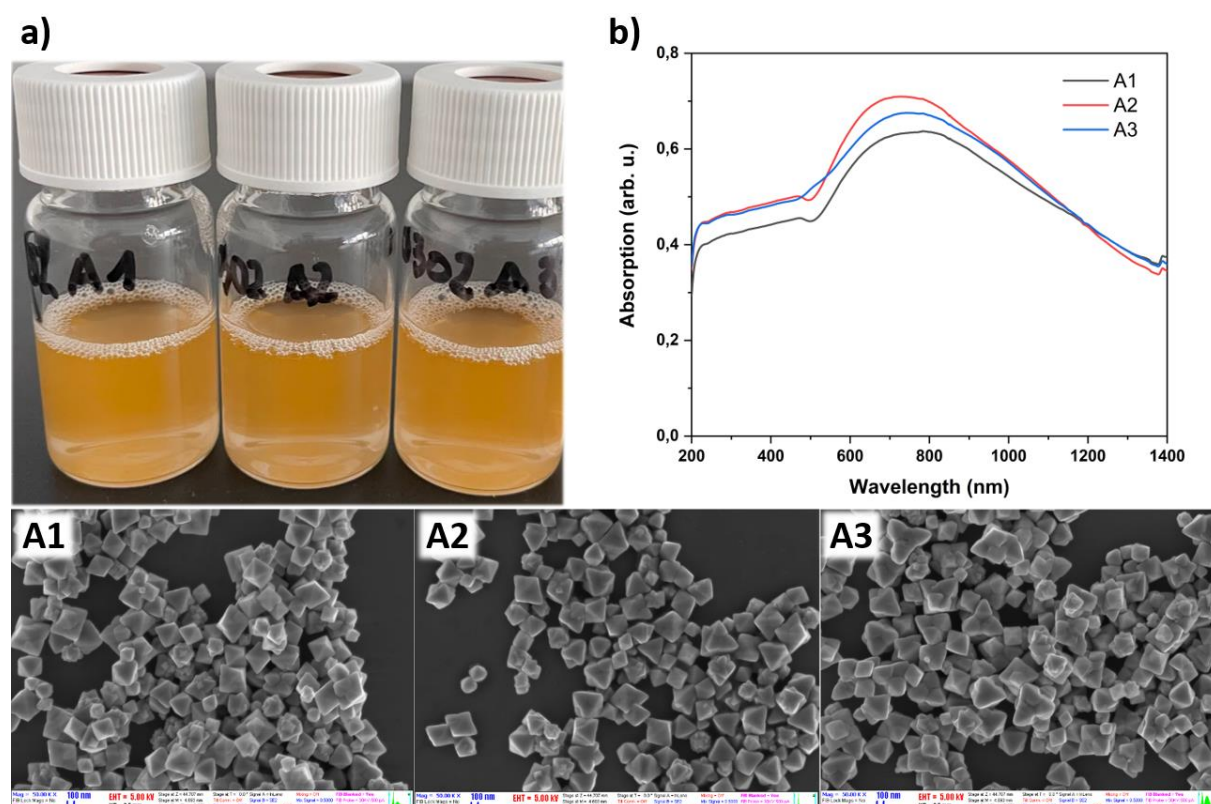

Figure 29. (a) The as synthesised particles, (b) the extinction spectra of the sample and (A1 – A3) representative SEM images related to the three samples.

Huang *et al.* used $Cu(NO_3)_2$, N_2H_4, and NaOH to fabricate octahedral Cu_2O NPs.[56] To reproduce their results, I carried out three parallel syntheses according to the paper. The colour of the as-synthesised products was identical, as well as the extinction spectra and the corresponding SEM images were very similar. It turned out to be a robust, reproducible synthesis that resulted in Cu_2O NPs with a narrow size distribution close to the desired size range. The major problem was with the shape of the particles, which was not uniform, their surface was rough, and the edges were roundish. The as-prepared particle solutions, the extinction spectra and the SEM images are shown in **Figure 30**.
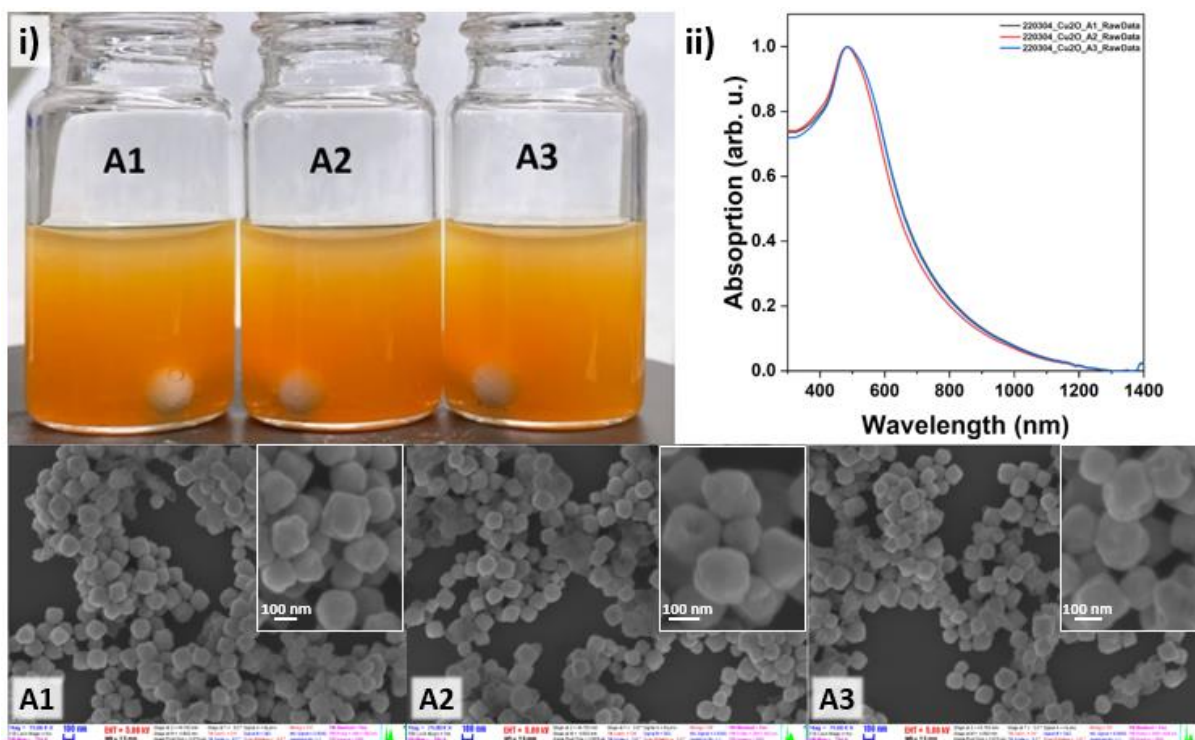
Figure 30. (*i*) The synthesised particles, (*ii*) the related extinction spectra and (*A1 – A3*) representative SEM images of the three samples.

In order to improve the particle morphology, I made a series of synthesis tuning the concentration of N_2H_4 while keeping all other parameters constant. The original recipe used 9.18 mL H_2O, 100 µL 0.1M $Cu(NO_3)_2$, 20 µL 1M NaOH and 700 µL N_2H_4. As a reference, I performed a synthesis according to the original recipe.

To cover a wide N_2H_4 concentration range, I made 7 more samples using the same quantity of $Cu(NO_3)_2$ and NaOH as those in the original recipe, but with the following amounts of N_2H_4 and H_2O: 200, 300, 400, 600, 630, 660 and 1000 µL of N_2H_4 and 9.68, 9.58, 9.48, 9.28, 9.25, 9.20 and 8.88 mL H_2O, respectively. The colour of all samples made by the modified recipe was the same as that of the reference. The extinction spectra were similar for each sample as well, except for the sample made using 300 µL N_2H_4, which showed a much narrower peak, indicating narrow size distribution and uniform particle shape. The extinction spectra and the related SEM images are shown in **Figure 31**.
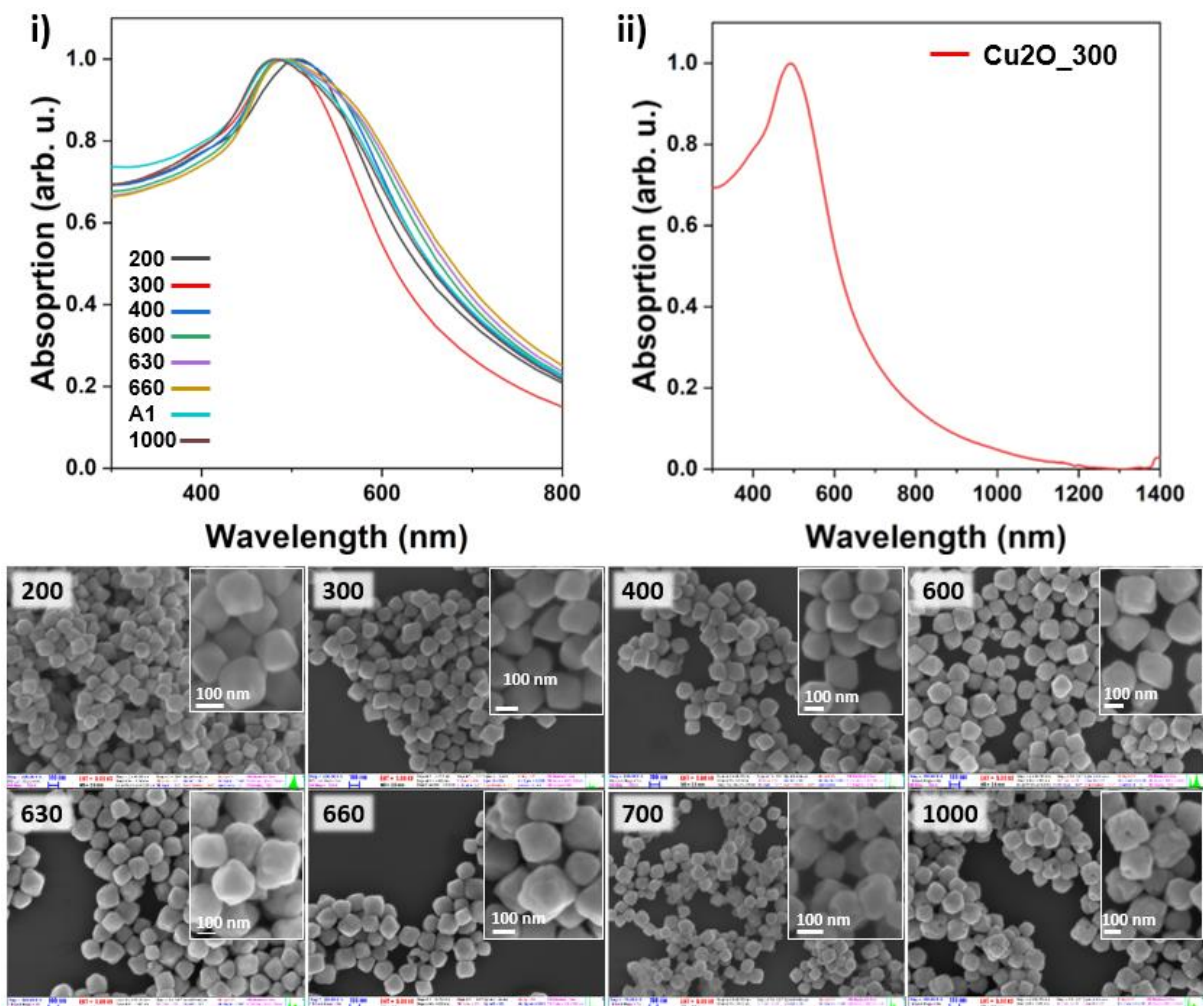
Figure 31. (*i*) Extinction spectra of the 8 samples made to investigate the effect of N_2H_4 quantity on the particle morphology, (*ii*) extinction spectra of the sample made by the addition of 300 μL N_2H_4 and (200 – 1000) representative SEM images of the different sample.

Increasing concentration of N_2H_4 resulted in the etching of the particles. In contrast, decreasing the amount of N_2H_4 resulted in significant improvement in the particle morphology. The particle surface was still rough in the case of the samples made by the addition of 600, 630 and 660 μL N_2H_4, however, the samples with addition of 300 and 400 μL N_2H_4 resulted in smooth surfaces. In the case of the sample made by the addition of 200 μL N_2H_4, the edges became roundish.

To fine-tune the shape of the particles, I made another series of synthesis finely adjusting the quantity of N_2H_4 around 300 μL (which I found to give the best result in the previous experiment). In this case, as a reference, I made a sample with the addition of 300 μL N_2H_4, and I made 6 more samples as the follows: 225, 250, 275, 325, 350, 375 μL N_2H_4 and 9.505, 9.530, 9.555, 9,605, 9.630, 9.655 mL H_2O was added (the concentration of $Cu(NO_3)_2$ and NaOH was constant). Again, the best result was achieved in the case of the sample made by the addition of 300 μL N_2H_4. The measured extinction spectra and the related SEM images are shown in **Figure 32**.
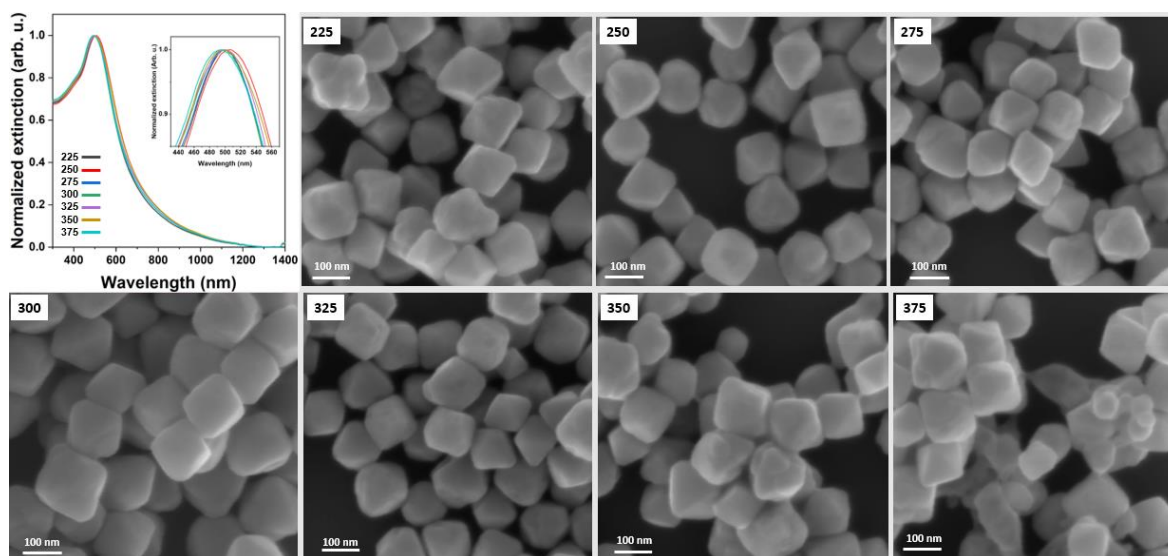
Figure 32. Fine-tuning the concentration of N_2H_4.

To check the reproducibility of the synthesis, and the stability of the particles three parallel syntheses using 300 µL N_2H_4 were carried out. The negligible difference in the extinction spectra between the three as-synthesised samples and the previously synthesised one indicates that the synthesis is robust and reproducible.
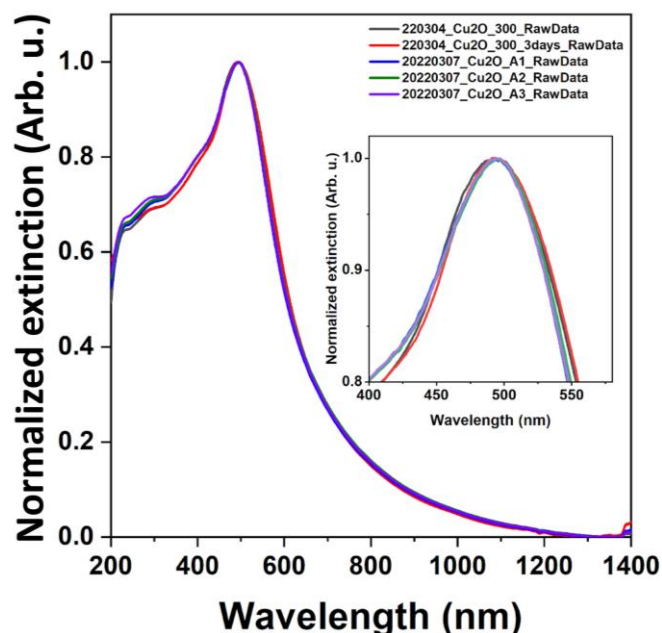

Figure 33. Extinction spectra of a previously synthesised octahedral Cu_2O NP sample after (black) and three days after the synthesis (red), and the spectra of the three as-synthesised samples made parallel (blue, green and purple).

For future experiments (gel formation), a larger amount of the sample is required. To this end, I attempted to scale up the synthesis using 91.8 mL H_2O, 1 mL 0.1 M $Cu(NO_3)_2$, 200 µL 1 M NaOH and 3 mL 0.2 M N_2H_4 (as it is described in chapter 3.2.1). I made two of the synthesis in parallel to check the reproducibility. The extinction spectra of the as-synthesised scaled-up

products were similar and did not show major difference compared to the spectra of the previously synthesised sample. To test the stability of the particles the spectra of the sample have been recorded over two months (**Figure 34**. f). The negligible difference in the spectra indicates the stability of the particles. Based on the SEM images I determined the average base edge length of the particles, which turned out to be around 136 nm.
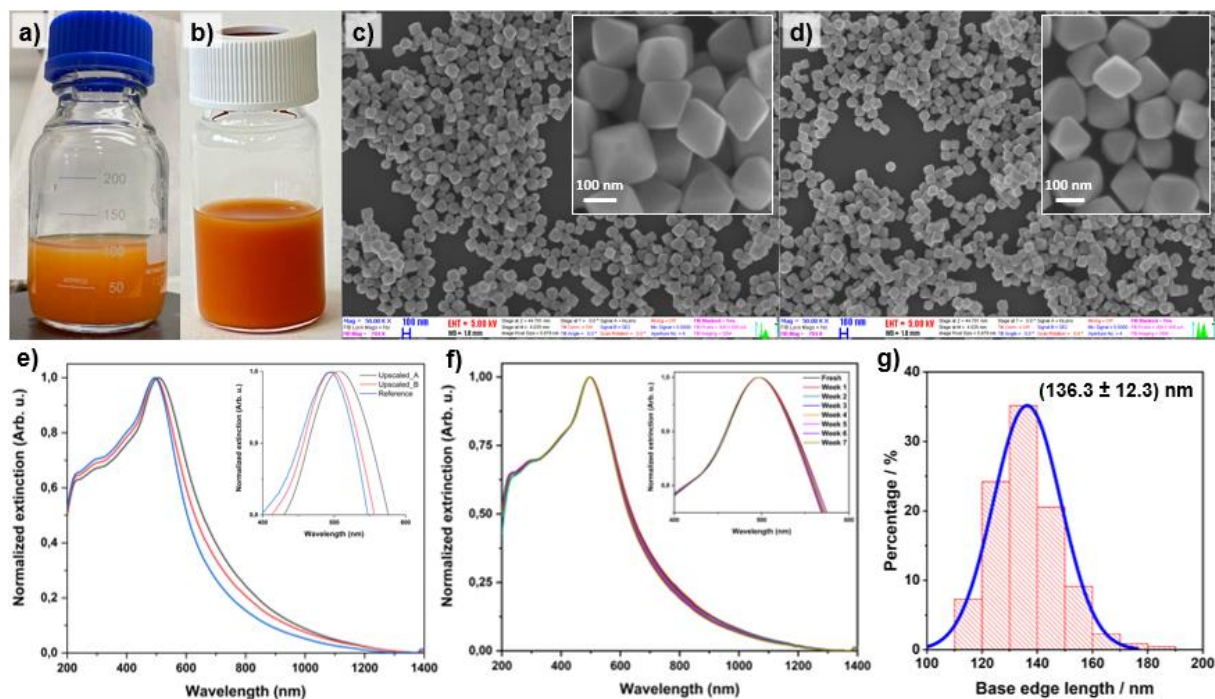

Figure 34. The scaled-up product (a) during the synthesis (aqueous solution) and (b) after the purification (ethanolic stock solution) of pristine Cu_2O nano octahedra. (c, d) Representative SEM images of the parallel-synthesised scaled-up products as well as (e) the extinction spectra belonging to the as synthesised scaled-up sample (black and red) and the reference (blue). (f) Extinction spectra recorded from the same sample represent the stability of the sample. (g) Size distribution of the scaled-up product (219 particles were measured).

Besides the SEM measurements, the elemental composition of the sample was measured with energy dispersive X-ray spectroscopy (EDS). The results of the EDS measurement verified the formation of the Cu_2O phase (1:2 Cu:O ratio); the slight O excess can be attributed to the oxide layer of the supporting Si and the absorbed ethanol molecules on the NPs. Table 4 contains the results of the measurements, and **Figure 35** shows one of the measurements.

Table 4. The results of the EDS measurements made on the scaled-up sample of the pristine Cu_2O octahedral NPs (in atomic %).

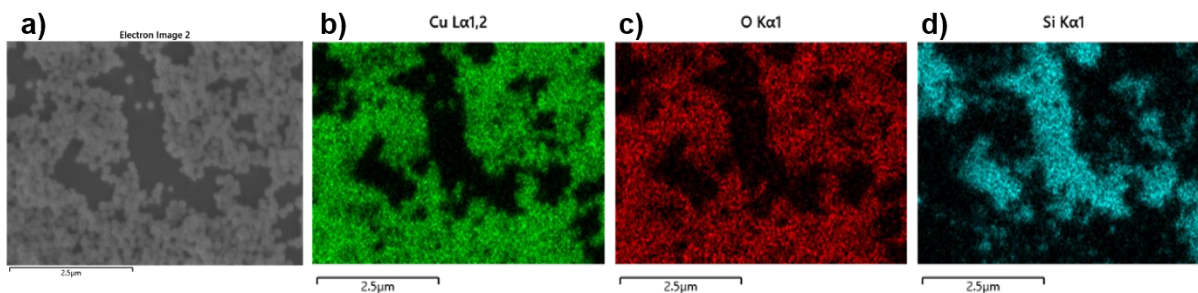| Map position	Cu	O	Si	Total
1	49.69	26.64	23.67	100.00
2	35.05	20.03	44.93	100.00

Figure 35. Analysis of the elemental composition of pristine Cu_2O octahedral NPs using EDS. (a) SEM image of the measured area, the EDS map of (b) copper, (c) oxygen and (d) silicon (which was the substrate of the sample)

4.1.2. Synthesis of gold nanorods

I synthesised gold nanorods as it is described in 3.2.2. Based on the SEM analysis, the dimensions of the synthesised AuNRs are as follows: the width is (27.6 ± 2.1) nm and the length is (81.3 ± 5.8) nm. This results in an average aspect ratio of 2.95. The peak position of its longitudinal plasmon mode is at 722 nm. The concentration of Au^0 can be determined from the intensity of the extinction spectrum at 400 nm. It resulted in $c^{Au(0)} = 0.3526$ mM. The narrow extinction band of the sample indicates narrow size distribution and uniform shaped particles, which are confirmed by the SEM analysis.
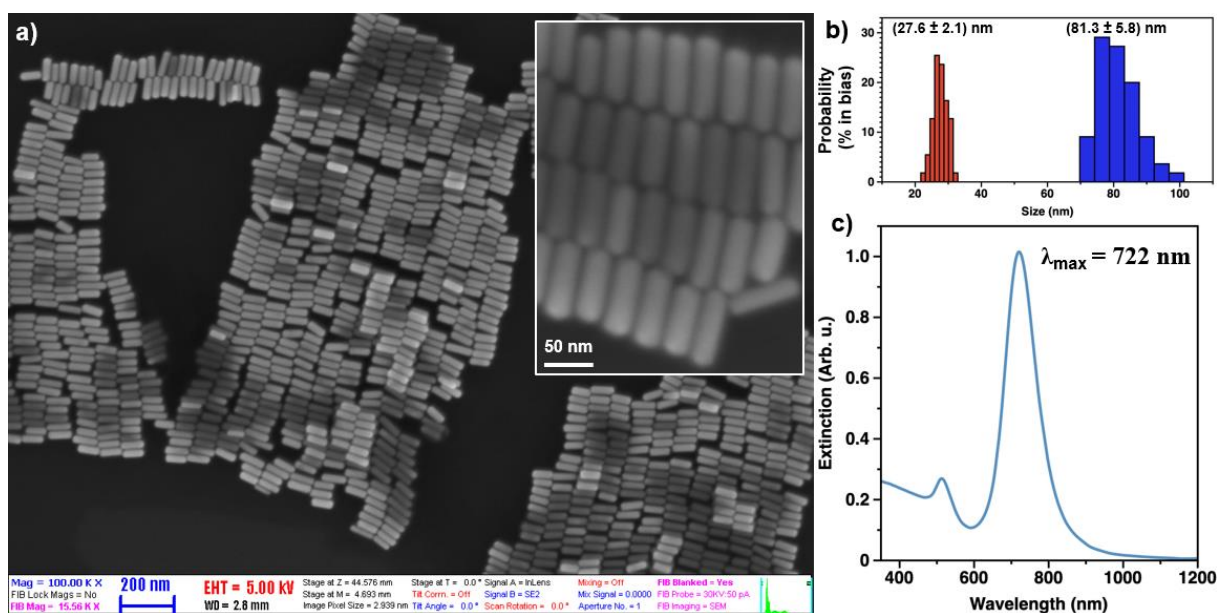

Figure 36. Synthesis of gold nanorods. (a) SEM image of the product, (b) the distribution of the width (red) and length (blue) of the particles and (c) the extinction spectrum of the sample.

4.1.3. Synthesis of AuNR@Cu₂O multicomponent nanoparticles

To fabricate AuNR@Cu₂O with dimensions approximately equal to those of the pristine Cu₂O nano octahedra, first, I made a series of synthesis using different amounts of AuNR seed particles to investigate the size controllability of the process. I added 0.5, 1, 2 and 3.5 mL $c^{Au(0)} = 0.6257$ mM AuNR solution to the growth solution to prepare *sample a – d*, respectively.
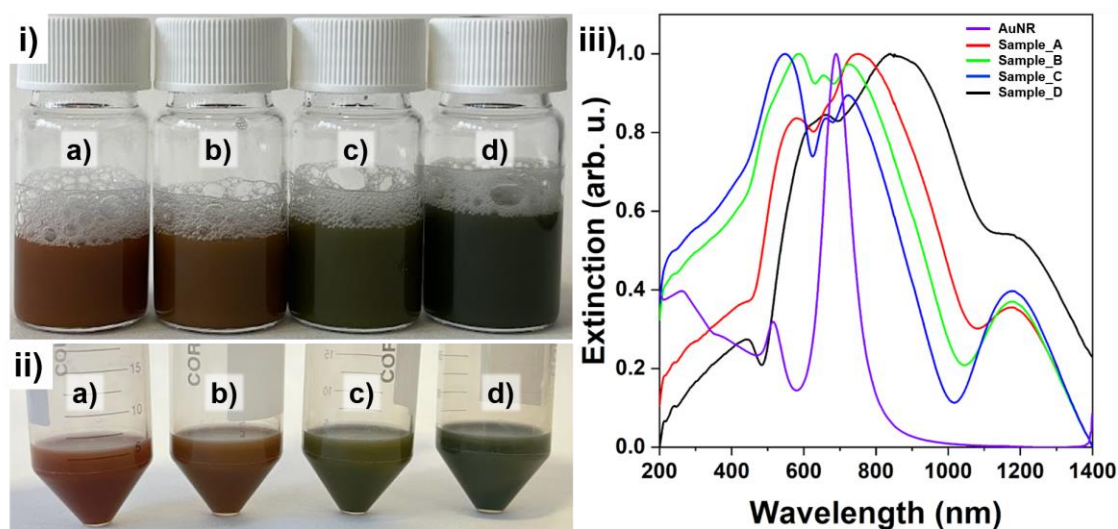

Figure 37. Synthesis of AuNR@Cu₂O. (*i*) During the synthesis and (*ii*) after the purification. (*iii*) The normalized extinction spectra the AuNRs (purple) and sample a – d: black, red, green and blue curves, respectively.

In principle, with increasing AuNR concentration the size of AuNR@Cu₂O decreases. It was confirmed by the SEM analysis of the samples (**Figure 38**):
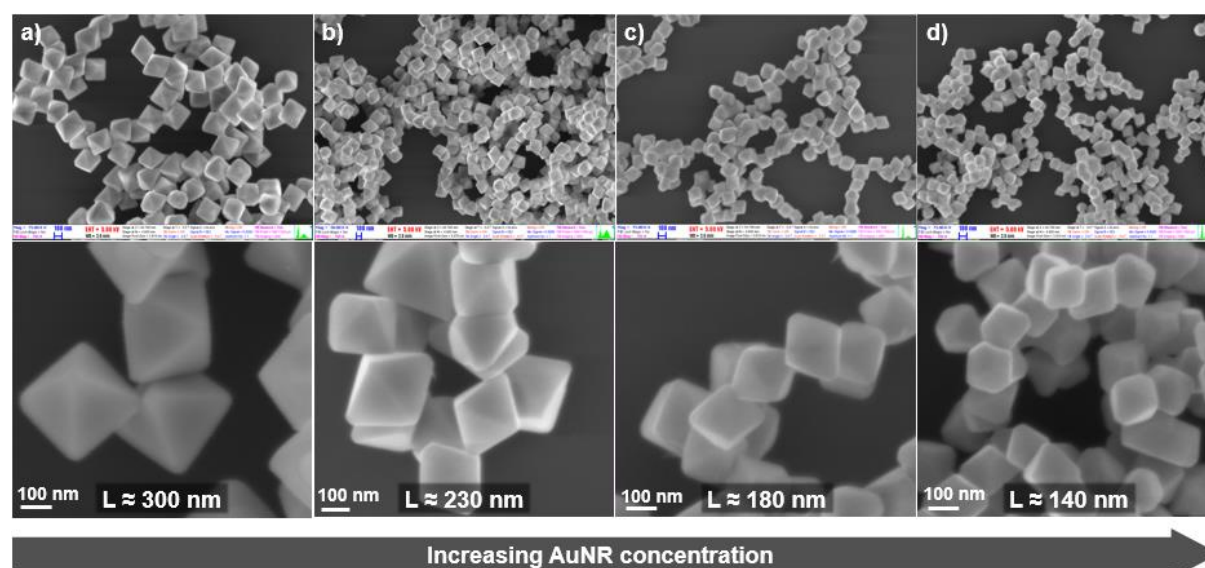

Figure 38. Size analysis of AuNR@Cu₂O core-shell heterostructured NPs.

I attempted to scale-up the synthesis using the procedure described in chapter 3.2.3, resulted in the ethanolic stock solution of AuNR@Cu$_2$O. The extinction spectra of the product were similar and did not show major difference compared to the spectra of the previously synthesised sample (**Figure 39. a**: green and blue lines). Based on the SEM images, I determined the average base edge length of the particles, which turned out to be around 137 nm. The atomic ratio of Cu:Au in the scaled-up AuNR@Cu$_2$O sample was determined with EDS and was found to be 38.62 ± 0.74.
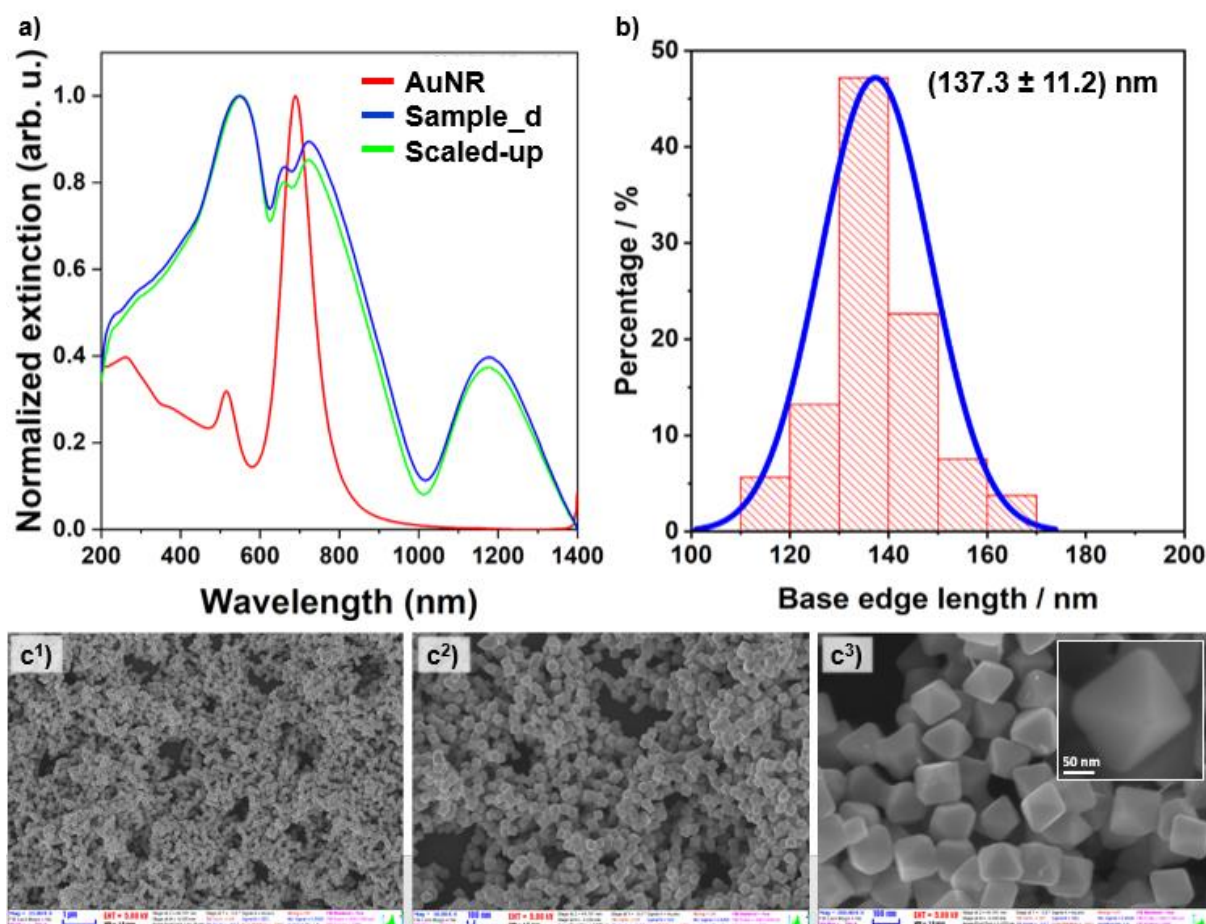

Figure 39. (a) Extinction spectra of the scaled-up (blue) and a previously synthesized (*sample d*, green) AuNR@Cu$_2$O. (b) Size distribution of the scaled-up product. (c) Representative SEM images made of the scaled-up product. The average particle size is around 137 nm (53 particles were measured).

Table 5. The results of EDS analysis made on the scaled-up sample of AuNR@Cu$_2$O in atomic %. (Figure 2. Ap.).

Position	C	O	Si	Cu	Au	Total	**Cu/Au**
1	6.64	27.22	0.64	63.88	1.62	100	**39.43**
2	6.43	26.2	5.79	60.01	1.58	100	**37.98**
3	6.96	27.05	3.29	61.11	1.59	100	**38.43**

4.1.4. Synthesis of Cu₂O@Au multicomponent nanoparticles

To decorate the pristine Cu_2O nano octahedra with gold nanograins, first, I made a series of synthesis to investigate how the most homogeneous and uniform decoration can be achieved. First, I varied the quantity of gold precursor in a wide range, while keeping all other parameters constant. The procedure was as follows: 0.25 mL concentrated ethanolic solution of the previously synthesised Cu_2O NPs was centrifuged, and the precipitate was redispersed in 2.5 mL H_2O. During intense shaking, I quickly injected 2.5 mL of 0.2 mM Au^{3+} solution into the Cu_2O particle solution. After 20 minutes of shaking, I centrifuged the sample at 4500 rpm for 5 minutes and redispersed the precipitate in 2.5 mL absolute ethanol. I repeated the same process with the injection of 0.08 mM, 0.04 mM, 0.02 mM and 0.01 mM of Au^{3+} solutions.

The increasing Au content causes a continuous blue shift and broadening in the extinction spectra (Figure **40** *ii*). In the case of *sample A*, which has the largest Au content, the spectral change is remarkable. Based on the SEM images, the significant spectral change of *sample A* (especially the experienced blue shift) can most likely be attributed to the etching of Cu_2O NPs by the increased Au content.[49] Reducing the Au^{3+} concentration facilitates the preservation of the original particle morphology, and a uniform decoration can be achieved for *sample C*. Lowering further the concentration of Au^{3+} leads to an increasing amount of partially decorated, or undecorated Cu_2O NPs. The elemental composition of *sample C* and *sample D* was analysed *via* EDS, which results are summarized in Table 6.
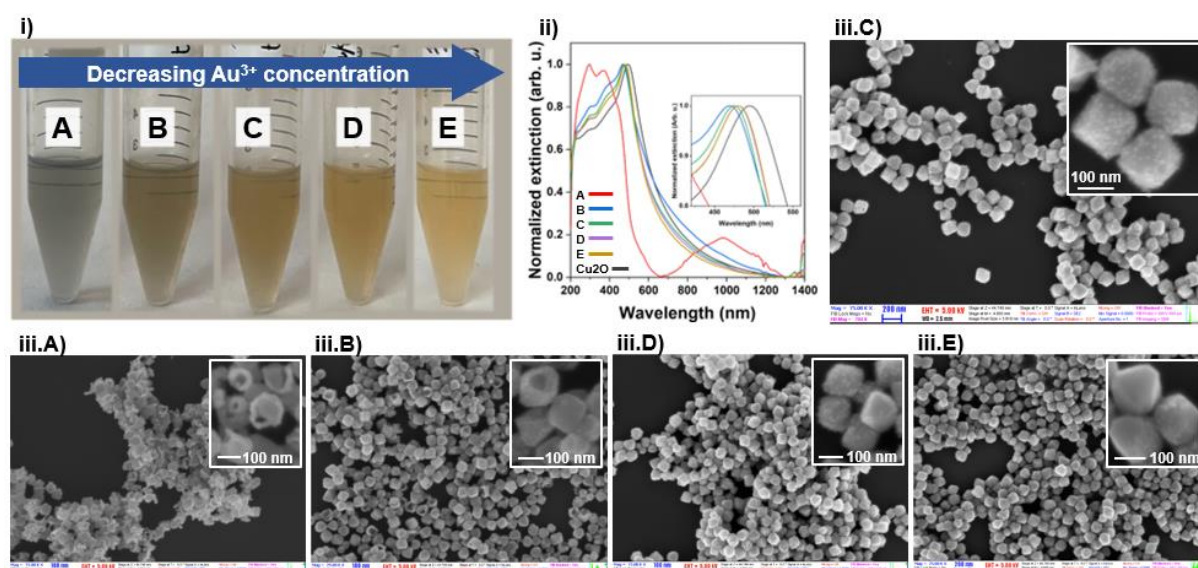

Figure **40**. (*i*) Solutions of Cu_2O@Au. The Au contend decreases from *sample A* to *sample E*. (*ii*) Extinction spectra of the synthesised Au decorated and pristine (black line) Cu_2O NPs. (*iii*) SEM images of the decorated NPs.

Table 6. The results of EDS measurements made on $Cu_2O@Au$ (in atomic%).

Sample	Au	Cu	O	Si	Total	**Cu/Au**
C	0.80	8.87	5.90	84.44	100.00	**11.09**
D	0.18	4.25	3.15	92.42	100.00	**23.61**

To fabricate $Cu_2O@Au$, with approximately an equal atomic ratio of Cu:Au to that of in AuNR@Cu_2O (around 39:1), I made another series of synthesis, to fine-tune the Au^{3+} concentration. To this end, I repeated the procedure, with the following concentrations of the injected Au^{3+} solutions: 0.020 mM, 0.018 mM, 0.016 mM, 0.014 mM, 0.0124 mM, 0.011 mM and 0.010 mM (*sample A* to *G*, respectively). Although, the extinction spectra do not show significant differences in this concentration range, the decoration was homogeneous only in the case of *sample D* and *E* according to the SEM images.
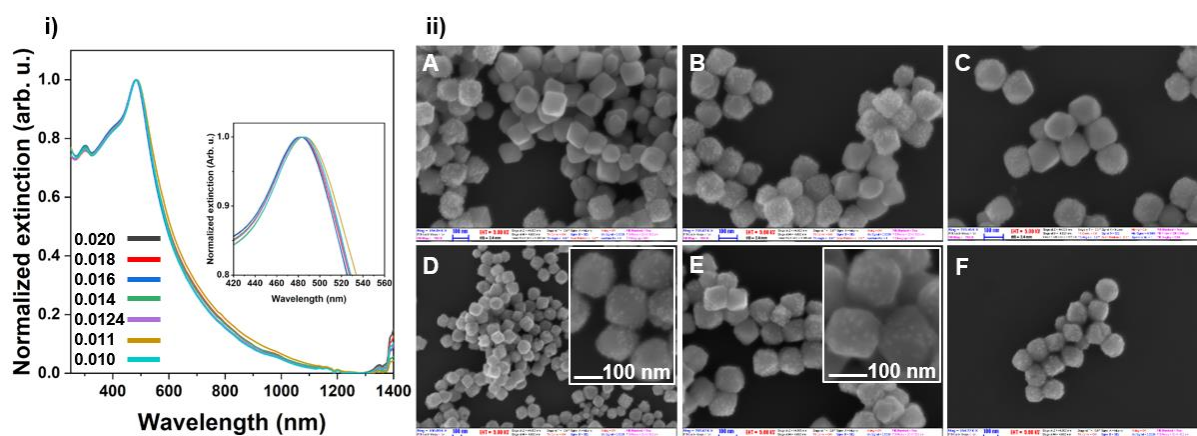

Figure 41. Fine-tuning the Au content in $Cu_2O@Au$. The corresponding (*i*) extinction spectra and (ii) SEM images.

I adjusted the concentration of the Au^{3+} solution to 0.0116 mM, and scaled-up the synthesis, as it is detailed in chapter 3.2.4, resulted in the ethanolic stock solution of $Cu_2O@Au$. The decoration resulted in the red shift and broadening of the extinction peak supporting the preservation of the initial octahedral shape and the deposition of the Au nanograins. Based on the SEM images, the decoration turned out to be homogeneous. The atomic ratio of Cu:Au in the scaled-up $Cu_2O@Au$ was determined with EDS: 39.94 ± 0.51. Based on the EDS measurements, I successfully achieved approximately the same atomic ratio of Cu:Au in the two different types of multicomponent nanoparticle systems, which became, thus, comparable.
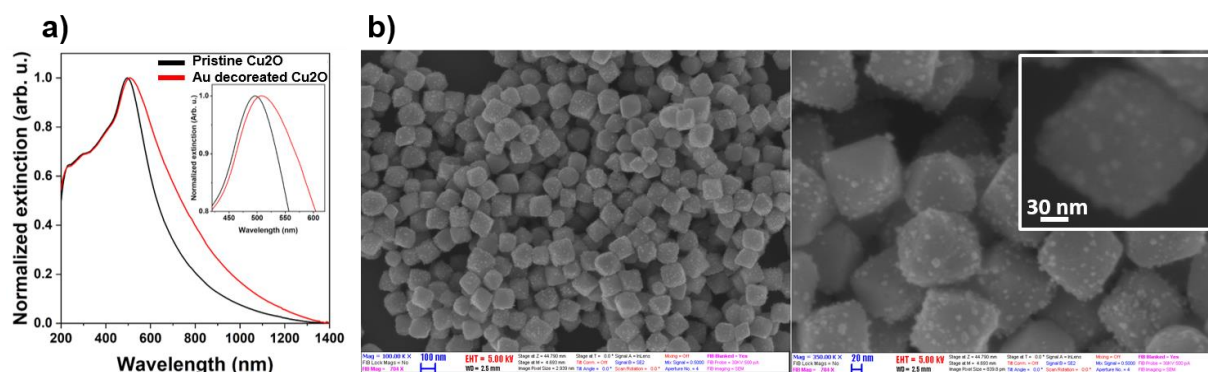
Figure 42. Scaled-up synthesis of Au nanograin decorated Cu_2O nano octahedra. (a) Extinction spectra and (b) representative SEM images of the sample.

Table 7. The results of EDS measurements made on the scaled-up $Cu_2O@Au$ sample in atomic % (**Figure 3. Ap.**).

Position	C	O	Si	Cu	Au	Total	Cu/Au
1	6.81	26.00	14.06	51.81	1.31	100	**39.55**
2	8.22	28.73	4.52	57.12	1.41	100	**40.51**
3	8.41	27.57	7.77	54.87	1.38	100	**39.76**

4.2. Structural characterisation of the nanoparticle building blocks

The copper concentration in the samples was accurately quantified using total reflection X-ray fluorescence. To this end, 50 µL of the ethanolic stock solution, 50 µL concentrated HNO_3 and 50 µL yttrium standard was added to 4850 µL H_2O. Table 8 summarizes the copper concentration in the different samples:

Table 8. TXRF results for the copper concentrations.

Sample	Ethanolic stock solutions	
	ppm	g / L
Pristine Cu_2O nano octahedra	453.0	0.453
AuNR@Cu_2O	1707.5	1.707
Cu_2O@Au	170.8	0.171

The phase and purity of particles was analysed with X-ray diffraction spectroscopy. To prepare the sample for the XRD measurement, I centrifuged 700 µL of the ethanolic stock solutions, removed 690 µL of the supernatant and then redispersed the precipitate *via* ultrasonication in the remaining 10 µL ethanol. I dropped 5 µL of the concentrated solution on top of a Si wafer, and then let the ethanol evaporate. The results of the XRD measurements are shown in **Figure 43**. The peaks with 2Θ values of 29.632°, 36.503°, 42.402°, 52.581°, 61.520°, 65.703°, 69.753°, 73.699° and 77.567° corresponds to the {110}, {111}, {200}, {211}, {220}, {221}, {310}, {311} and {222} crystal planes of Cu_2O, respectively. The peaks with 2Θ values of 38.188°, 44.386°, 64.578° and 77.569° corresponds to the {111}, {200}, {220} and {311} crystal planes of gold, respectively.

The diffraction patterns of the pristine Cu_2O nano octahedra were identical over 48 days, indicating the stability of the NPs (**Figure 43**. a.). In the case of the pristine Cu_2O nano octahedra, the intense peak at 36.503° confirms that the particles are primarily bounded by {111} facets. Although, the presence of the weak {110}, {200} and {220} peaks indicate that the particles' shape is not perfectly octahedral but slightly truncated. In the case of the heterostructured NPs, the relative intensity of the {111} peak becomes less dominant. For the AuNR@Cu_2O it may be attributed to the presence of the AuNR, which may induce crystal defects structure of the Cu_2O shell, thereby, increasing the relative intensity of the other peaks. For Cu_2O@Au, the intensity of the {111} peak becomes even smaller implying the effect of the deposition process: through galvanic reaction the reducing Au^{3+} ions may etch the surface of the Cu_2O NPs during the growth of the nanograins. In the case of AuNR@Cu_2O, the {111} and {200} peaks are characteristic for the facets at the tips of the AuNR. The gold nanograins

cannot be detected with XRD, due to the small size of the domains. The diffraction patterns do not contain unidentified peaks, which indicates the purity of the samples.
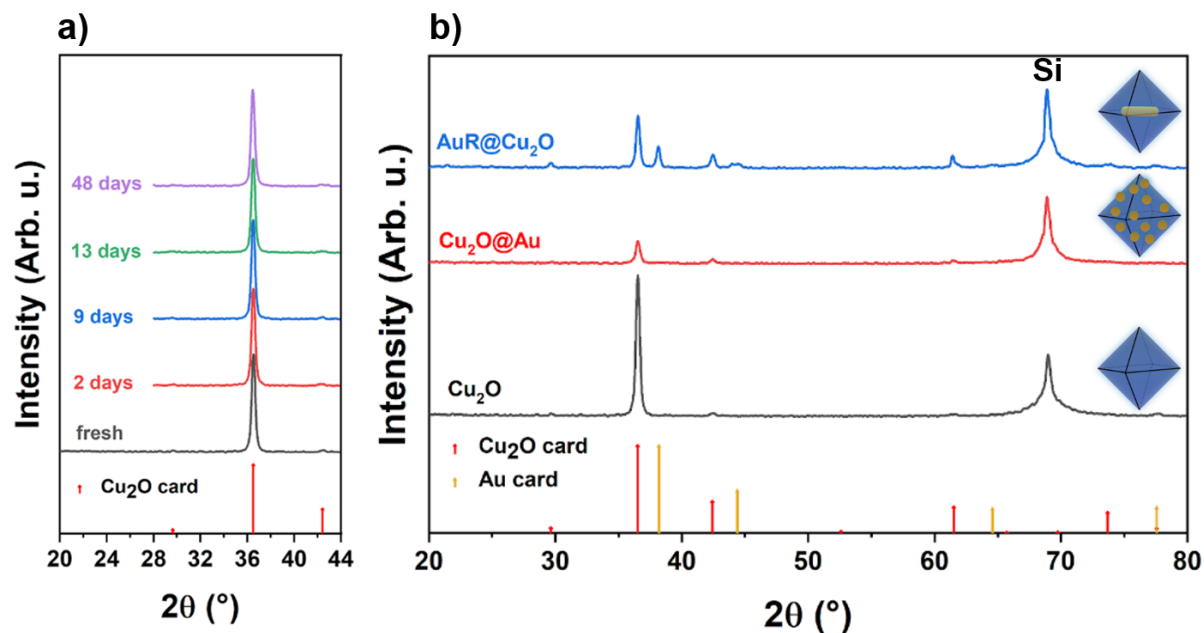

Figure 43. Results of the X-ray diffraction analysis. (a) Investigating the stability of the pristine Cu_2O nano octahedra: XRD patterns of the same sample after the synthesis, as well as 2, 9, 13 and 48 days after the synthesis. (b) XRD diffractograms of the pristine Cu_2O and the multicomponent NPs. The data cards of Cu_2O and Au are in the appendices (Figure 4. Ap.). The intense peak at 69.2° 2Θ angle in all samples is attributed to the silicon substrate.

The crystal structure of single NPs was investigated with transmission electron microscopy, as well as by elemental composition analysis, using an EDS detector coupled to the TEM.

The TEM measurements confirm that the shape of the Cu_2O NPs is not perfectly octahedral, moreover, its clearly visible, that the crystal structure is not perfect, particularly in the case of the dark field images of the pristine Cu_2O nano octahedra, in which patches can be observed (**Figure 44**). The patches may indicate voids inside or at the surface of the particle. This assumption is supported by the EDS measurements, in which the intensity of copper drops at the patches. In the case of AuNR@Cu_2O, the TEM images shows stress-induced crystal defects in the Cu_2O shell, which manifest themselves as line defects pointing towards the AuNR core. Moreover, in the region of the nanorod core, the Moiré effect of the different unit cells (*i.e.* Au and Cu_2O) also appears (**Figure 45**). In the case of the Cu_2O@Au, the size of the gold nanograins can be determined based on the TEM images and was found to be around 6-8 nm. Moreover, the TEM images confirm, that there is an atomic connection between the Cu_2O and the deposited Au nanograins (**Figure 46**) and the growth is most probably epitaxial.
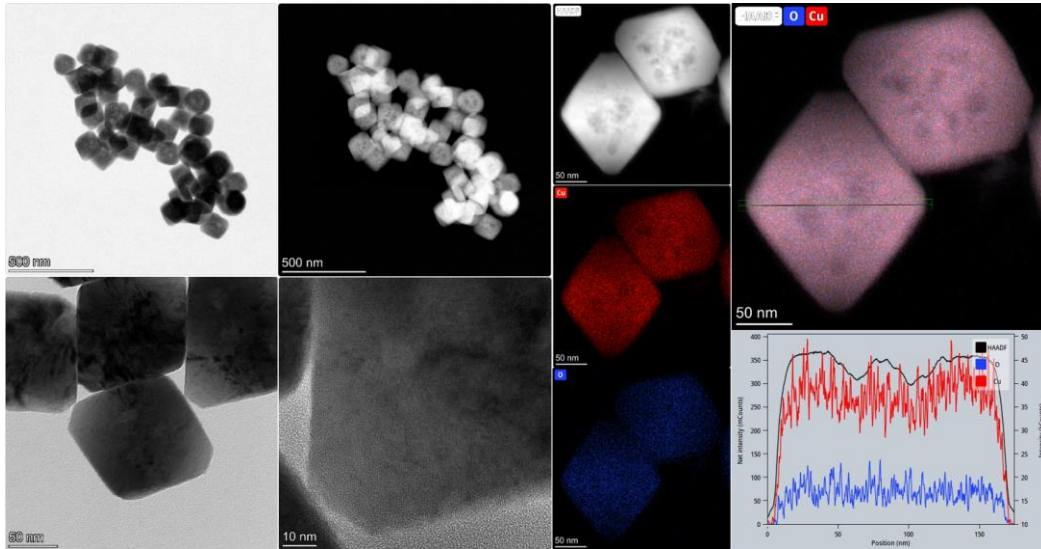
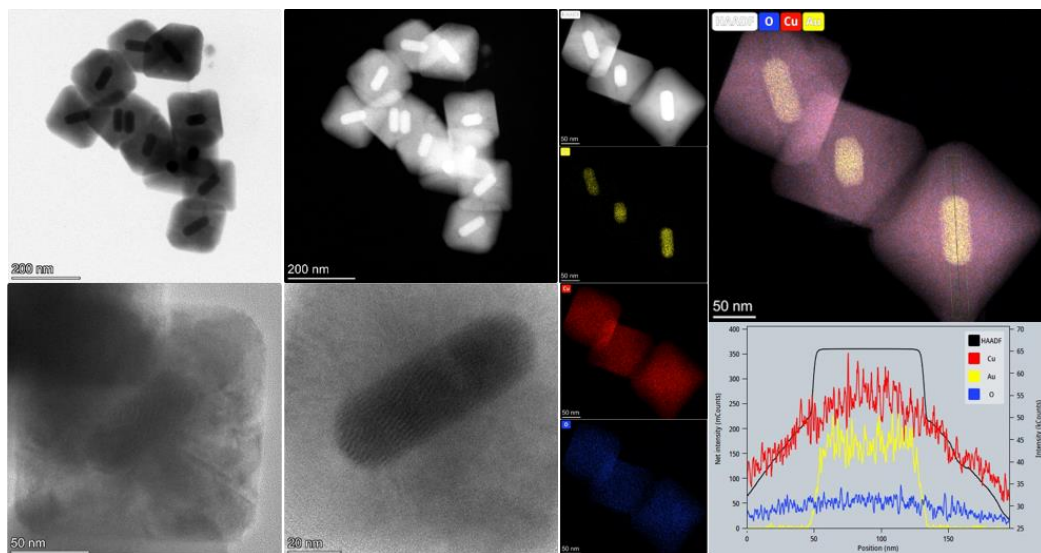**Figure 44.** TEM images and EDS measurements of pristine Cu$_2$O octahedral NPs.

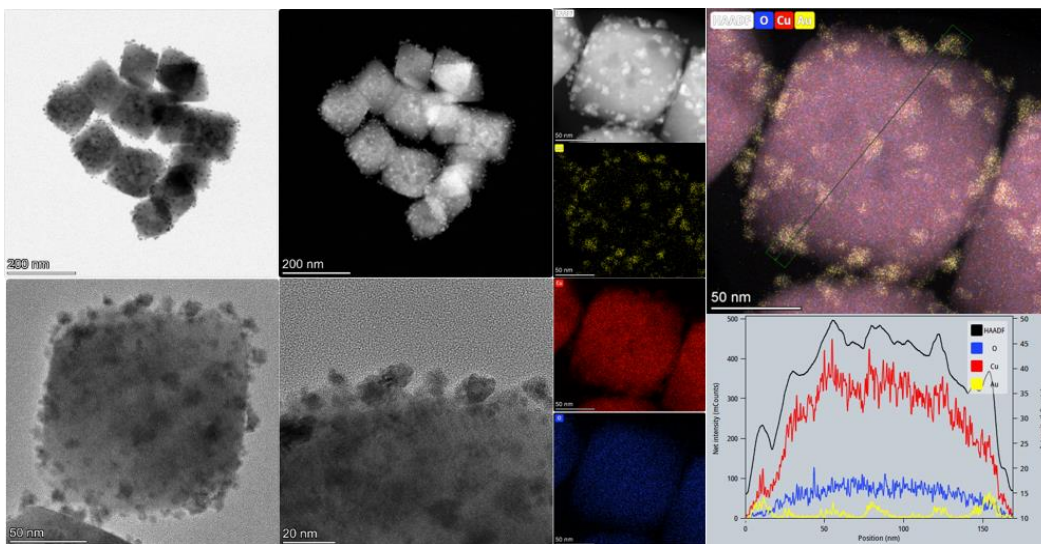**Figure 45.** TEM images and EDS measurements of AuNR@Cu$_2$O core-shell NPs.

Figure 46. TEM images and EDS measurements of Au nanograin decorated Cu$_2$O NPs

4.3. Optical characterisation of the nanoparticle building blocks

To investigate and compare the optical properties of the three different nano systems, namely, the pristine Cu_2O nano octahedra, the AuNR@Cu_2O and the Cu_2O@Au, I prepared samples with equal concentration of copper (0.5 mM equals to 0.0318 g/L) based on Table *8*. Absorption spectra of the samples were recorded in the integrating sphere of the Edinburgh FS5 spectrofluorometer using the synchronous "absorptance" mode calculating the pure absorption from the diffuse reflectance.

The position of them main peak of the extinction spectrum of the pristine Cu_2O nano octahedron is located at 497 nm, which belongs to the superposition of the excitonic transition and the scattering peak maximum. The decoration with Au nanograins resulted in a slight redshift as well as in the broadening of the extinction peak. Moreover, the decoration resulted in an increased absorption beyond 500 nm in the visible range (**Figure 47**. a.). In the case of the core-shell structured NPs, the position of the main extinction peak suffered significant redshift to 580 nm. The longitudinal peak position of the AuNR significantly redshifted as well: from the original 722 nm to 1200 nm. The absorption of the AuNR@Cu_2O NPs remarkably increased in the visible range (**Figure 47**. b.)

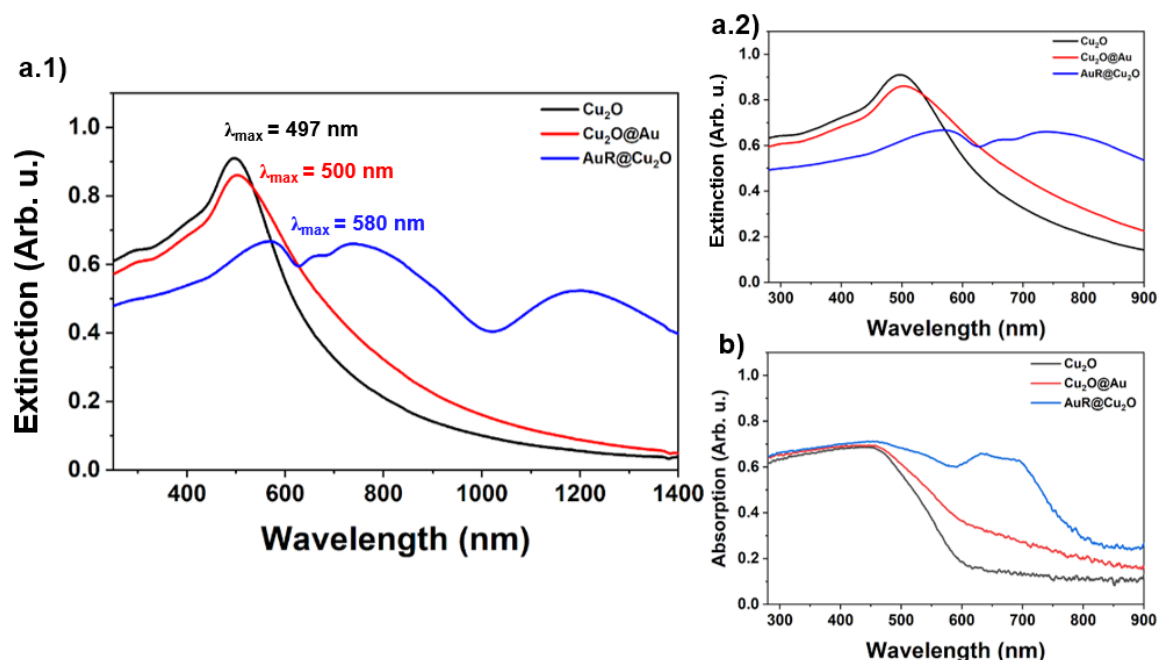**Figure 47.** (a) Extinction and (b) absorption spectra of pristine Cu_2O nano octahedra (black), AuNR@Cu_2O (blue) and Cu_2O@Au (red) with 0.5 mM copper concentration in all samples.

The PL emission spectrum of the pristine Cu_2O nano octahedra shows two peaks, which positions are at 508 nm and 585 nm (**Figure 48**. a.). To record the excitation spectra, I applied these 508 nm and 585 nm of emission wavelengths (**Figure 48**. b and c.), as well as for the

time-correlated single photon counting (TCSPC) measurements (**Figure 49**). During the TCSPC measurements, the samples were excited by a pulsed LED source ($\lambda = 320$ nm) with a repetition rate of 1 MHz. The decay curves were fit using biexponential fitting functions for all the measured samples indicating the contribution of two main radiative processes.

In the case of $Cu_2O@Au$, the intensity of the PL spectrum decreased compared to the spectrum of the pristine Cu_2O nano octahedra. I measured another $Cu_2O@Au$ sample with more Au content as well, which resulted in an even more decreased PL intensity (data are not shown). In case of $AuNR@Cu_2O$, the intensity of the PL spectrum further decreased. The decreased PL intensity is probably attributed to the increased charge separation by the gold NPs. Furthermore, the decrease in the PL intensity of $AuNR@Cu_2O$ compared to $Cu_2O@Au$ could also be attributed to the stress-induced crystal defects in the Cu_2O shell, in which the crystal defects act as traps for the charge carriers, promoting the non-radiative recombination pathways. From the characteristics of the excitation spectra, it can be concluded that the presence of gold does not alter the excitation behaviour of the samples, but its efficiency decreases from pristine to $Cu_2O@Au$ to $AuNR@Cu_2O$.

Based on the TCSPC measurements, the presence of gold decreases the lifetime at the 508 nm peak maximum for both $AuNR@Cu_2O$ and $Cu_2O@Au$, which effect implies an enhanced charge-carrier separation by the gold nanoparticles. The PL peak maximum at 585 nm can be attributed to the trap states in the oxide crystal. In the case of $Cu_2O@Au$, the crystal structure of the Cu_2O nano octahedra is not modified, the slight decrease of the lifetime may be attributed to the charge separation effect of the Au nanograins. In the case of the $AuNR@Cu_2O$, the lifetime increases at the 585 nm peak maximum, which is probably the effect of the increased amount of trap states due to the line defects in the Cu_2O shell.
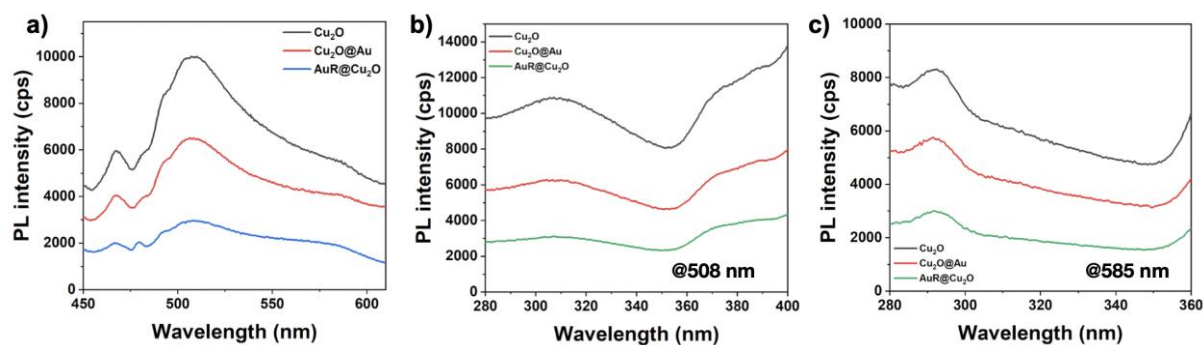

Figure 48. Photoluminescence measurements of pristine Cu_2O nano octahedra (black), $AuNR@Cu_2O$ (green) and $Cu_2O@Au$ (red and blue) with 0.5 mM copper concentration in all samples. (a) Excitation spectra and emission spectra with (b) 508 nm and (c) 585 nm excitation wavelengths.
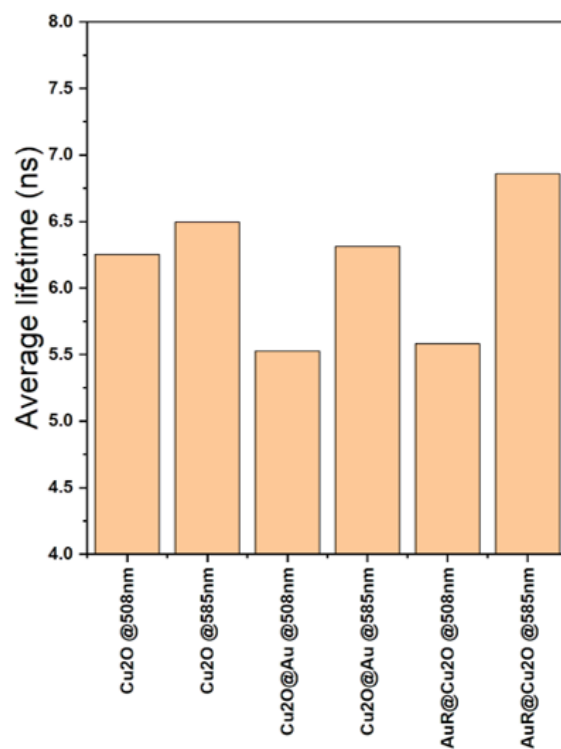
Figure 49. Results of the time-correlated single photon counting measurements of (a, b) pristine Cu_2O nano octahedra, (c, d) AuNR@ and (e, f) Cu_2O@Au at excitation wavelengths of (a, c, e) 508 nm and (b, d, f) 585 nm. The copper concentration was 0.5 mM in all samples (Figure 5. Ap.).

4.4. Preparation of cryoaerogels

To fabricate monolithic cryoaerogels using the synthesised NPs, I prepared highly concentrated aqueous solutions from the ethanolic stock solutions: approximately 5 g/L of the pristine Cu_2O octahedral NPs and another, 30 g/L of the pristine Cu_2O octahedral NPs, 24 g/L of AuNR@Cu_2O and 32 g/L of Cu_2O@Au. I injected 20 µL of those solutions into liquid nitrogen filled glass vials, and then quickly put them in the refrigerated vacuum chamber of a laboratory built lyophilizer (designed and built based on a sputter coater in the research group, **Figure 50**). I left them for 4 hours at 200 µbar vacuum to let the water ice sublimate. Previous experiments showed that pure water ice can entirely be sublimated using these lyophilization parameters.

Figure 50. The instrument used for the freeze-drying process: the low pressure (200 µbar) is provided by a dry scroll vacuum pump attached to a vacuum chamber. The cooling during the freeze-drying is achieved by a Peltier thermoelectric module ($\Delta T = 108°C$), attached to a condenser providing a large surface for the condensation of water. The hot side of the Peltier was chilled through a water-cooled plate.

The freeze-drying process is shown in **Figure 51**. a. The nitrogen freezes due to the decreased pressure (first minute in the image), and then sublimates in a few minutes. After 4 hours of freeze drying, although the monoliths suffer some shrinkage, the process end up in porous objects (**Figure 51** b-d.). I fixed small fragments of the cryogels on a SEM pin stub using conductive silver ink, and the samples were analysed with SEM (**Figure 51 .e.**), Figure 6. Ap., Figure 7. Ap., Figure 8. Ap.).

The first sample, made from the 5 g/L pristine Cu_2O NP solution collapsed before the freeze-drying finished. This observation indicates that a minimum NP concentration is required to obtain a stable aerogel structure with sufficient mechanical stability. The shrinkage during the freeze-drying may indicate that the NP concentration is not high enough, resulting in an insufficient interconnection between the NPs or they sheet-like substructures. However, the higher NP concentration facilitates macrostructures with significantly less shrinkage. Furthermore, the SEM images show a well interconnected porous microstructure, where the sheets consist of the individual nanoparticles with preserved morphology.
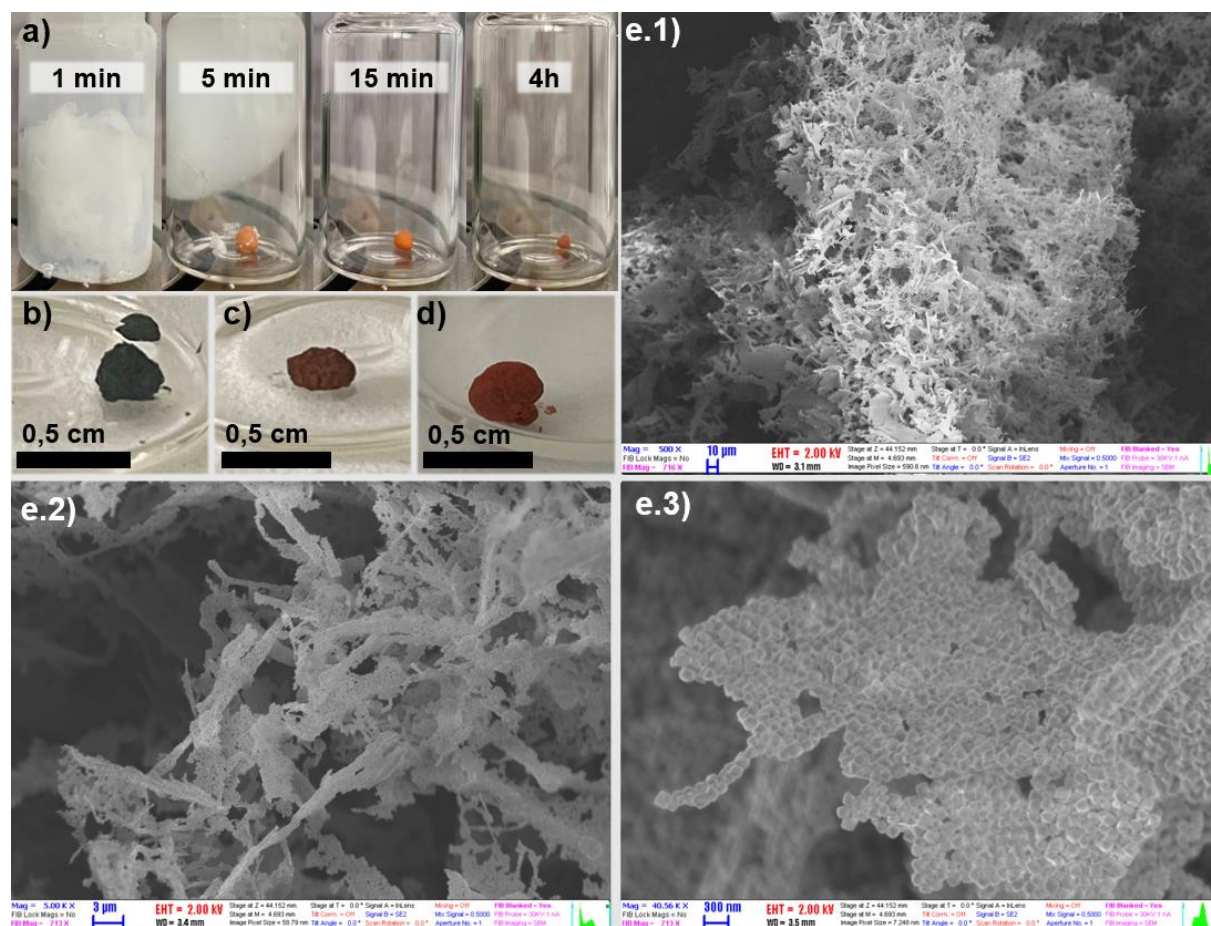

Figure 51. (a) Freeze-drying process in time. The monolith cryogel product made from the (b) pristine Cu_2O nano octahedra, (c) AuNR@Cu_2O and (d) Cu_2O@Au. (e) Representative SEM images of the cryogel product in the case of the pristine Cu_2O. SEM images of the cryogels made from AuNR@Cu_2O and Cu_2O@Au are in the appendices: Figure 6. Ap., Figure 7. Ap. and Figure 8. Ap.

5. Summary

Using wet-chemical approaches, I synthesised pristine Cu_2O nano octahedra, in high yield, narrow size distribution with an average base edge length of 136 nm, in a reproducible way. Using a seed-mediated process, I synthesised gold nanorods with average dimensions of (81×28) nm. *Via* growing octahedral Cu_2O onto the gold nanorods, and depositing gold nanograins onto the pristine Cu_2O nano octahedra, I fabricated two different heterostructured, multicomponent nanoparticle systems: (i) core-shell structured gold nanorod – Cu_2O octahedra, and (ii) Au nanograin-decorated Cu_2O octahedra, respectively. The fabricated heterostructured NPs have the same dimensions as that of the pristine Cu_2O nano octahedra, moreover, they possess approximately the same atomic ratio of copper and gold. The octahedral Cu_2O and its gold heterostructures were in the focus of my research to reveal the optical and structural properties.

The presence of gold led to the decrease in the photoluminescence intensity for both the core-shell and the decorated heterostructured NPs compared to the pure Cu_2O NPs. The lowered PL intensity is probably attributed to charge carrier separation enhancement in the heterostructures as a result of the synergy of the components. This assumption is supported by the results of the PL lifetime measurements. Comparing the heterostructured NP systems, it can be concluded that the relative position of the gold has a significant impact on the optical properties of the system. The presence of gold was significantly more dominant in the form of a gold nanorod than as in the form of nanograins: the nanograin decoration has solely resulted in a slight shift and broadening of the absorption and extinction spectra. In contrast, the gold nanorods have significantly modified the optical properties, causing large broadening and orders of magnitude larger peak shifts including the plasmonic features of the embedded NRs. The effect of gold nanorods was also significantly higher on the PL properties and resulted in a more intense quenching. Even though the quantity of gold in the two heterostructured systems is approximately the same, gold alters the optical properties in the form of a nanorod more significantly. This includes the presence of the localised surface plasmon resonance, in contrary to the nanograins, whose size is under the LSPR limit. Furthermore, the growth of the Cu_2O phase is also influenced by the presence of the gold nanorod, which might induce the formation of crystal defects and stress having an impact on the non-radiative recombination of the carriers.

Using the NP building blocks, I successfully fabricated well interconnected highly porous macroscopic cryoaerogels. Tuning the parameters of the cryogelation process (particle concentration, drying time), all the three nanosystems were able to be converted into cryogel monoliths which opens the way towards novel photocatalytic applications.

References

(1)   Sanchez, F.; Sobolev, K. Nanotechnology in Concrete – A Review. *Constr. Build. Mater.* **2010**, *24* (11), 2060–2071. https://doi.org/10.1016/j.conbuildmat.2010.03.014.

(2)   *Nanophysics and Nanotechnology: An Introduction to Modern Concepts in Nanoscience*.

(3)   Schaak, R. E.; Steimle, B. C.; Fenton, J. L. Made-to-Order Heterostructured Nanoparticle Libraries. *Acc. Chem. Res.* **2020**, *53* (11), 2558–2568. https://doi.org/10.1021/acs.accounts.0c00520.

(4)   Liu, X.; Iocozzia, J.; Wang, Y.; Cui, X.; Chen, Y.; Zhao, S.; Li, Z.; Lin, Z. Noble Metal–Metal Oxide Nanohybrids with Tailored Nanostructures for Efficient Solar Energy Conversion, Photocatalysis and Environmental Remediation. *Energy Environ. Sci.* **2017**, *10* (2), 402–434. https://doi.org/10.1039/C6EE02265K.

(5)   Yuan, L.; Geng, Z.; Xu, J.; Guo, F.; Han, C. Metal-Semiconductor Heterostructures for Photoredox Catalysis: Where Are We Now and Where Do We Go? *Adv. Funct. Mater.* **2021**, *31* (27), 2101103. https://doi.org/10.1002/adfm.202101103.

(6)   Trindade, T.; O'Brien, P.; Pickett, N. L. Nanocrystalline Semiconductors: Synthesis, Properties, and Perspectives. *Chem. Mater.* **2001**, *13* (11), 3843–3858. https://doi.org/10.1021/cm000843p.

(7)   Heinemann, M.; Eifert, B.; Heiliger, C. Band Structure and Phase Stability of the Copper Oxides Cu 2 O, CuO, and Cu 4 O 3. *Phys. Rev. B* **2013**, *87* (11), 115111. https://doi.org/10.1103/PhysRevB.87.115111.

(8)   Rej, S.; Bisetto, M.; Naldoni, A.; Fornasiero, P. Well-Defined Cu2O Photocatalysts for Solar Fuels and Chemicals. *J. Mater. Chem. A* **2021**, *9* (10), 5915–5951. https://doi.org/10.1039/D0TA10181H.

(9)   Hsu, S.-W.; Rodarte, A. L.; Som, M.; Arya, G.; Tao, A. R. Colloidal Plasmonic Nanocomposites: From Fabrication to Optical Function. *Chem. Rev.* **2018**, *118* (6), 3100–3120. https://doi.org/10.1021/acs.chemrev.7b00364.

(10)   Eustis, S.; El-Sayed, M. A. Why Gold Nanoparticles Are More Precious than Pretty Gold: Noble Metal Surface Plasmon Resonance and Its Enhancement of the Radiative and Nonradiative Properties of Nanocrystals of Different Shapes. *Chem. Soc. Rev.* **2006**, *35* (3), 209–217. https://doi.org/10.1039/B514191E.

(11)   Amendola, V.; Pilot, R.; Frasconi, M.; Maragò, O. M.; Iatì, M. A. Surface Plasmon Resonance in Gold Nanoparticles: A Review. *J. Phys. Condens. Matter* **2017**, *29* (20), 203002. https://doi.org/10.1088/1361-648X/aa60f3.

(12)   Pelton, M.; Bryant, G. W. *Introduction to metal-nanoparticle plasmonics*. Wiley : Science Wise Publishing: Hoboken, New Jersey, 2013.

(13)   Fedoruk, M. Plasmonic Manipulation of Thermoresponsive and Thermosetting Polymers. PhD Thesis, 2013.

(14)   Gergely-Fülöp, E. Preparation and Investigation of Nano-Sized Au/Silica Particle Composites. PhD Thesis, Budapest University of Technology and Economics, Budapest, 2014.

(15)   Foerster, B.; Rutten, J.; Pham, H.; Link, S.; Sönnichsen, C. Particle Plasmons as Dipole Antennas: State Representation of Relative Observables. *J. Phys. Chem. C* **2018**, *122* (33), 19116–19123. https://doi.org/10.1021/acs.jpcc.8b06350.

(16)   *Advances in optoplasmonic sensors – combining optical nano/microcavities and photonic crystals with plasmonic nanostructures and nanoparticles*. https://www.degruyter.com/document/doi/10.1515/nanoph-2017-0064/html (accessed 2022-05-11).

(17)   Jayabal, S.; Pandikumar, A.; Lim, H. N.; Ramaraj, R.; Sun, T.; Huang, N. M. A Gold Nanorod-Based Localized Surface Plasmon Resonance Platform for the Detection of Environmentally Toxic Metal Ions. *Analyst* **2015**, *140* (8), 2540–2555. https://doi.org/10.1039/C4AN02330G.

(18)   Link, S.; Mohamed, M. B.; El-Sayed, M. A. Simulation of the Optical Absorption Spectra of Gold Nanorods as a Function of Their Aspect Ratio and the Effect of the Medium Dielectric Constant. *J. Phys. Chem. B* **1999**, *103* (16), 3073–3077. https://doi.org/10.1021/jp990183f.

(19) Chang, H.-H.; Murphy, C. J. Mini Gold Nanorods with Tunable Plasmonic Peaks beyond 1000 Nm. *Chem. Mater.* **2018**, *30* (4), 1427–1435. https://doi.org/10.1021/acs.chemmater.7b05310.

(20) Bai, S.; Jiang, J.; Zhang, Q.; Xiong, Y. Steering Charge Kinetics in Photocatalysis: Intersection of Materials Syntheses, Characterization Techniques and Theoretical Simulations. *Chem. Soc. Rev.* **2015**, *44* (10), 2893–2939. https://doi.org/10.1039/C5CS00064E.

(21) Clavero, C. Plasmon-Induced Hot-Electron Generation at Nanoparticle/Metal-Oxide Interfaces for Photovoltaic and Photocatalytic Devices. *Nat. Photonics* **2014**, *8* (2), 95–103. https://doi.org/10.1038/nphoton.2013.238.

(22) Lee, J. B.; Choi, S.; Kim, J.; Nam, Y. S. Plasmonically-Assisted Nanoarchitectures for Solar Water Splitting: Obstacles and Breakthroughs. *Nano Today* **2017**, *16*, 61–81. https://doi.org/10.1016/j.nantod.2017.08.008.

(23) Wu, K.; Chen, J.; McBride, J. R.; Lian, T. Efficient Hot-Electron Transfer by a Plasmon-Induced Interfacial Charge-Transfer Transition. *Science* **2015**, *349* (6248), 632–635. https://doi.org/10.1126/science.aac5443.

(24) Zhang, N.; Han, C.; Fu, X.; Xu, Y.-J. Function-Oriented Engineering of Metal-Based Nanohybrids for Photoredox Catalysis: Exerting Plasmonic Effect and Beyond. *Chem* **2018**, *4* (8), 1832–1861. https://doi.org/10.1016/j.chempr.2018.05.005.

(25) Cushing, S. K.; Li, J.; Bright, J.; Yost, B. T.; Zheng, P.; Bristow, A. D.; Wu, N. Controlling Plasmon-Induced Resonance Energy Transfer and Hot Electron Injection Processes in Metal@TiO$_2$ Core–Shell Nanoparticles. *J. Phys. Chem. C* **2015**, *119* (28), 16239–16244. https://doi.org/10.1021/acs.jpcc.5b03955.

(26) Linic, S.; Christopher, P.; Ingram, D. B. Plasmonic-Metal Nanostructures for Efficient Conversion of Solar to Chemical Energy. *Nat. Mater.* **2011**, *10* (12), 911–921. https://doi.org/10.1038/nmat3151.

(27) Chen, Y.; Munechika, K.; Jen-La Plante, I.; Munro, A. M.; Skrabalak, S. E.; Xia, Y.; Ginger, D. S. Excitation Enhancement of CdSe Quantum Dots by Single Metal Nanoparticles. *Appl. Phys. Lett.* **2008**, *93* (5), 053106. https://doi.org/10.1063/1.2956391.

(28) Ray, K.; Badugu, R.; Lakowicz, J. R. Distance-Dependent Metal-Enhanced Fluorescence from Langmuir−Blodgett Monolayers of Alkyl-NBD Derivatives on Silver Island Films. *Langmuir* **2006**, *22* (20), 8374–8378. https://doi.org/10.1021/la061058f.

(29) Bek, A.; Jansen, R.; Ringler, M.; Mayilo, S.; Klar, T. A.; Feldmann, J. Fluorescence Enhancement in Hot Spots of AFM-Designed Gold Nanoparticle Sandwiches. *Nano Lett.* **2008**, *8* (2), 485–490. https://doi.org/10.1021/nl072602n.

(30) Naiki, H.; Masuo, S.; Machida, S.; Itaya, A. Single-Photon Emission Behavior of Isolated CdSe/ZnS Quantum Dots Interacting with the Localized Surface Plasmon Resonance of Silver Nanoparticles. *J. Phys. Chem. C* **2011**, *115* (47), 23299–23304. https://doi.org/10.1021/jp207997j.

(31) Munechika, K.; Chen, Y.; Tillack, A. F.; Kulkarni, A. P.; Plante, I. J.-L.; Munro, A. M.; Ginger, D. S. Spectral Control of Plasmonic Emission Enhancement from Quantum Dots near Single Silver Nanoprisms. *Nano Lett.* **2010**, *10* (7), 2598–2603. https://doi.org/10.1021/nl101281a.

(32) Mishra, N. Metal–Semiconductor Hybrid Nano-Heterostructures for Photocatalysis Application. In *Semiconductor Photocatalysis - Materials, Mechanisms and Applications*; Cao, W., Ed.; InTech, 2016. https://doi.org/10.5772/62636.

(33) Tsai, Y.-H.; Chanda, K.; Chu, Y.-T.; Chiu, C.-Y.; Huang, M. H. Direct Formation of Small Cu$_2$O Nanocubes, Octahedra, and Octapods for Efficient Synthesis of Triazoles. *Nanoscale* **2014**, *6* (15), 8704. https://doi.org/10.1039/C4NR02076F.

(34) Ke, W.-H.; Hsia, C.-F.; Chen, Y.-J.; Huang, M. H. Synthesis of Ultrasmall Cu$_2$O Nanocubes and Octahedra with Tunable Sizes for Facet-Dependent Optical Property Examination. *Small* **2016**, *12* (26), 3530–3534. https://doi.org/10.1002/smll.201600064.

(35) Wang, Z. L. Transmission Electron Microscopy of Shape-Controlled Nanocrystals and Their Assemblies. *J. Phys. Chem. B* **2000**, *104* (6), 1153–1175. https://doi.org/10.1021/jp993593c.

(36) Huang, W.-C.; Lyu, L.-M.; Yang, Y.-C.; Huang, M. H. Synthesis of Cu$_2$O Nanocrystals from Cubic to Rhombic Dodecahedral Structures and Their Comparative Photocatalytic Activity. *J. Am. Chem. Soc.* **2012**, *134* (2), 1261–1267. https://doi.org/10.1021/ja209662v.

(37) Leng, M.; Yu, C.; Wang, C. Polyhedral Cu2O Particles: Shape Evolution and Catalytic Activity on Cross-Coupling Reaction of Iodobenzene and Phenol. *CrystEngComm* **2012**, *14* (24), 8454. https://doi.org/10.1039/c2ce26295a.

(38) Xing, W.; Meng, F.; Yu, R. Atomic Structure of the Cu $_2$ O(111) Surface: A Transmission Electron Microscopy and DFT + *U* Study. *Phys. Status Solidi B* **2021**, *258* (10), 2100185. https://doi.org/10.1002/pssb.202100185.

(39) Zhu, S.; Deng, D.; Nguyen, M. T.; Chau, Y. R.; Wen, C.-Y.; Yonezawa, T. Synthesis of Au@Cu2O Core–Shell Nanoparticles with Tunable Shell Thickness and Their Degradation Mechanism in Aqueous Solutions. *Langmuir* **2020**. https://doi.org/10.1021/acs.langmuir.0c00382.

(40) Xue, J.; Shao, M.; Shen, Q.; Liu, X.; Jia, H. Facile and Time-Saving Synthesis of Octahedral Cu $_2$ O Crystals by an Ethanol-Assisted Solution Method at Low Temperatures. *CrystEngComm* **2017**, *19* (9), 1258–1264. https://doi.org/10.1039/C7CE00021A.

(41) Xu, H.; Wang, W.; Zhu, W. Shape Evolution and Size-Controllable Synthesis of Cu $_2$ O Octahedra and Their Morphology-Dependent Photocatalytic Properties. *J. Phys. Chem. B* **2006**, *110* (28), 13829–13834. https://doi.org/10.1021/jp061934y.

(42) Chen, H.; Shao, L.; Li, Q.; Wang, J. Gold Nanorods and Their Plasmonic Properties. *Chem. Soc. Rev.* **2013**, *42* (7), 2679–2724. https://doi.org/10.1039/C2CS35367A.

(43) Ye, X.; Zheng, C.; Chen, J.; Gao, Y.; Murray, C. B. Using Binary Surfactant Mixtures To Simultaneously Improve the Dimensional Tunability and Monodispersity in the Seeded Growth of Gold Nanorods. *Nano Lett.* **2013**, *13* (2), 765–771. https://doi.org/10.1021/nl304478h.

(44) Kong, L.; Chen, W.; Ma, D.; Yang, Y.; Liu, S.; Huang, S. Size Control of Au@Cu $_2$ O Octahedra for Excellent Photocatalytic Performance. *J Mater Chem* **2012**, *22* (2), 719–724. https://doi.org/10.1039/C1JM13672K.

(45) Zhu, J.; Lu, N.; Chen, W.; Kong, L.; Yang, Y.; Ma, D.; Huang, S. Influence of Au Nanoparticle Shape on Au@Cu $_2$ O Heterostructures. *J. Nanomater.* **2015**, *2015*, 1–9. https://doi.org/10.1155/2015/389790.

(46) Liu, X.-W. Selective Growth of Au Nanoparticles on (111) Facets of Cu $_2$ O Microcrystals with an Enhanced Electrocatalytic Property. *Langmuir* **2011**, *27* (15), 9100–9104. https://doi.org/10.1021/la2020447.

(47) Zhu, H.; Du, M.; Yu, D.; Wang, Y.; Zou, M.; Xu, C.; Fu, Y. Selective Growth of Au Nanograins on Specific Positions (Tips, Edges and Facets) of Cu2O Octahedrons to Form Cu2O–Au Hierarchical Heterostructures. *Dalton Trans.* **2012**, *41* (45), 13795. https://doi.org/10.1039/c2dt31487h.

(48) Zhu, H.; Du, M.; Yu, D.; Wang, Y.; Wang, L.; Zou, M.; Zhang, M.; Fu, Y. A New Strategy for the Surface-Free-Energy-Distribution Induced Selective Growth and Controlled Formation of Cu $_2$ O–Au Hierarchical Heterostructures with a Series of Morphological Evolutions. *J Mater Chem A* **2013**, *1* (3), 919–929. https://doi.org/10.1039/C2TA00591C.

(49) Chen, R.; Lu, J.; Liu, S.; Zheng, M.; Wang, Z. The Preparation of Cu2O@Au Yolk/Shell Structures for Efficient Photocatalytic Activity with a Self-Generated Acid Etching Method. *J. Mater. Sci.* **2018**, *53* (3), 1781–1790. https://doi.org/10.1007/s10853-017-1614-4.

(50) Rusch, P.; Zámbó, D.; Bigall, N. C. Control over Structure and Properties in Nanocrystal Aerogels at the Nano-, Micro-, and Macroscale. *Acc. Chem. Res.* **2020**, *53* (10), 2414–2424. https://doi.org/10.1021/acs.accounts.0c00463.

(51) Czömpöly, O.; Börcsök, E.; Groma, V.; Pollastri, S.; Osán, J. Characterization of Unique Aerosol Pollution Episodes in Urban Areas Using TXRF and TXRF-XANES. *Atmospheric Pollut. Res.* **2021**, *12* (11), 101214. https://doi.org/10.1016/j.apr.2021.101214.

(52) Https://Thebiologynotes.Com/Microscope/.

(53) Mankovskii, G.; Pejović-Milić, A. Total Reflection X-Ray Fluorescence Based Quantification of Gold Nanoparticles in Cancer Cells. *J. Anal. At. Spectrom.* **2018**, *33* (3), 395–403. https://doi.org/10.1039/C7JA00332C.

(54) Saada, T. N.; Pang, L.; Sravan Kumar, K.; Dourado, A. H. B.; Germano, L. D.; Vicentini, E. D.; Batista, A. P. L.; de Oliveira-Filho, A. G. S.; Dumeignil, F.; Paul, S.; Wojcieszak, R.; Melinte, S.; Sandu, G.; Petretto, G.; Rignanese, G.-M.; Braga, A. H.; Rosado, T. F.; Meziane, D.; Boukherroub, R.; de Torresi, S. I. C.; da Silva, A. G. M.; Szunerits, S. The Importance of the Shape of Cu2O

Nanocrystals on Plasmon-Enhanced Oxygen Evolution Reaction in Alkaline Media. *Electrochimica Acta* **2021**, *390*, 138810. https://doi.org/10.1016/j.electacta.2021.138810.

(55) Pastrián, F. A. C.; da Silva, A. G. M.; Dourado, A. H. B.; de Lima Batista, A. P.; de Oliveira-Filho, A. G. S.; Quiroz, J.; de Oliveira, D. C.; Camargo, P. H. C.; Córdoba de Torresi, S. I. Why Could the Nature of Surface Facets Lead to Differences in the Activity and Stability of Cu2O-Based Electrocatalytic Sensors? *ACS Catal.* **2018**, *8* (7), 6265–6272. https://doi.org/10.1021/acscatal.8b00726.

(56) Huang, J.-Y.; Madasu, M.; Huang, M. H. Modified Semiconductor Band Diagrams Constructed from Optical Characterization of Size-Tunable Cu $_2$ O Cubes, Octahedra, and Rhombic Dodecahedra. *J. Phys. Chem. C* **2018**, *122* (24), 13027–13033. https://doi.org/10.1021/acs.jpcc.8b02169.

Appendices
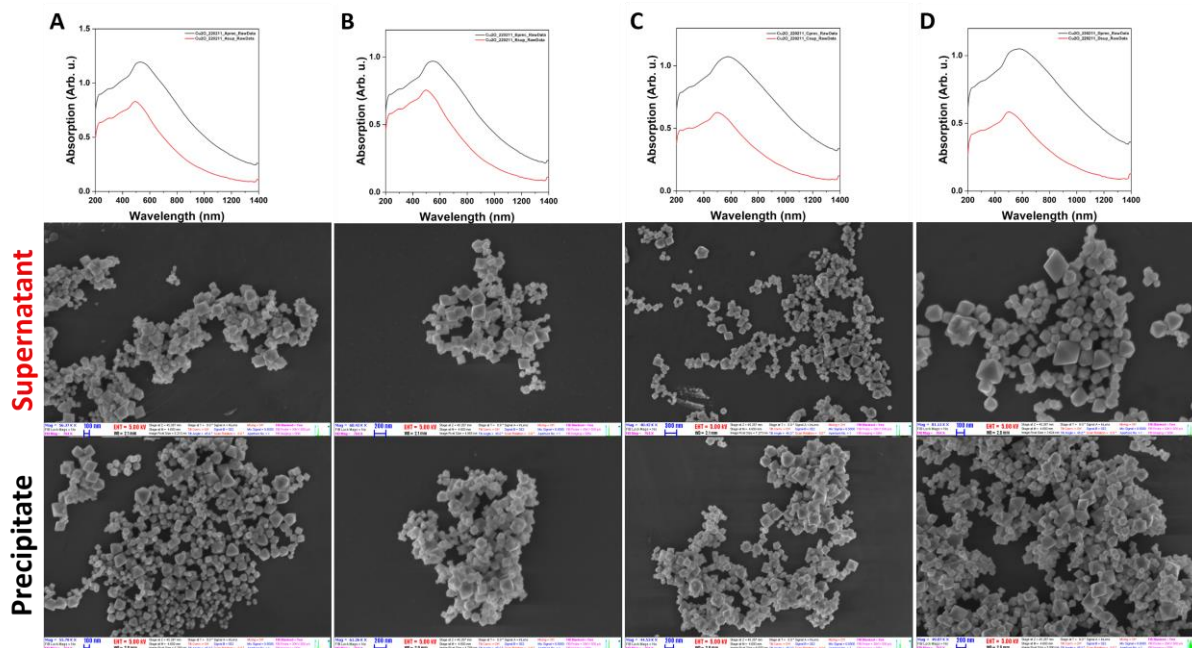
Figure 1. Ap. Extinction spectra of the supernatant and precipitate of the particles that was synthesised according to Ke *et al.* and the related SEM images.
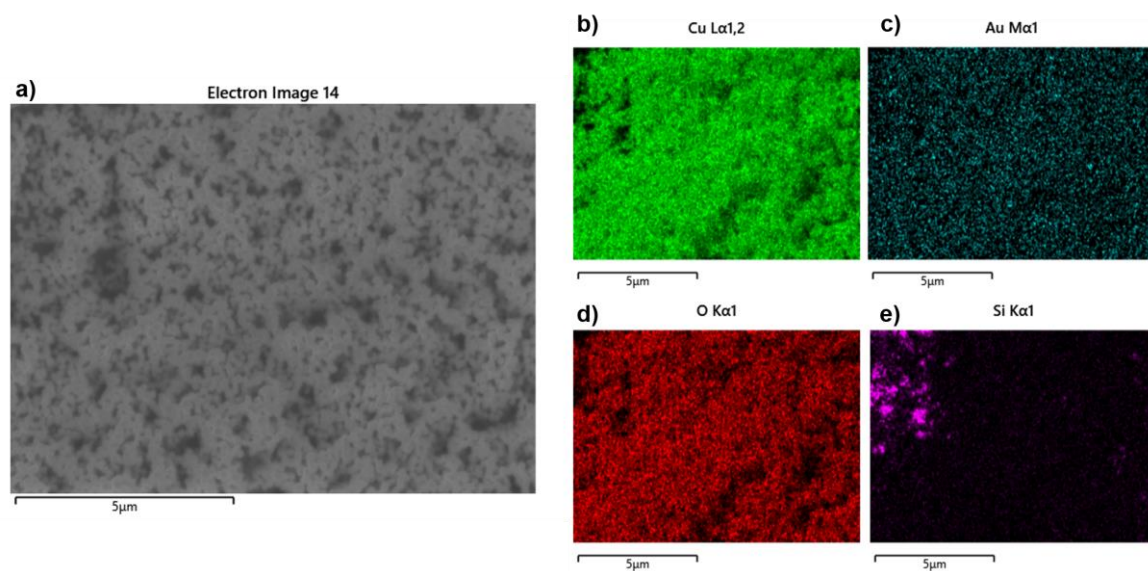

Figure 2. Ap. Analysing the elemental composition of the scaled-up AuNR@Cu$_2$O core-shell heterostructured NPs using EDS. (a) SEM image of the measured area, and the EDS map of (b) copper, (d) oxygen, (d) oxygen and (e) silicon.
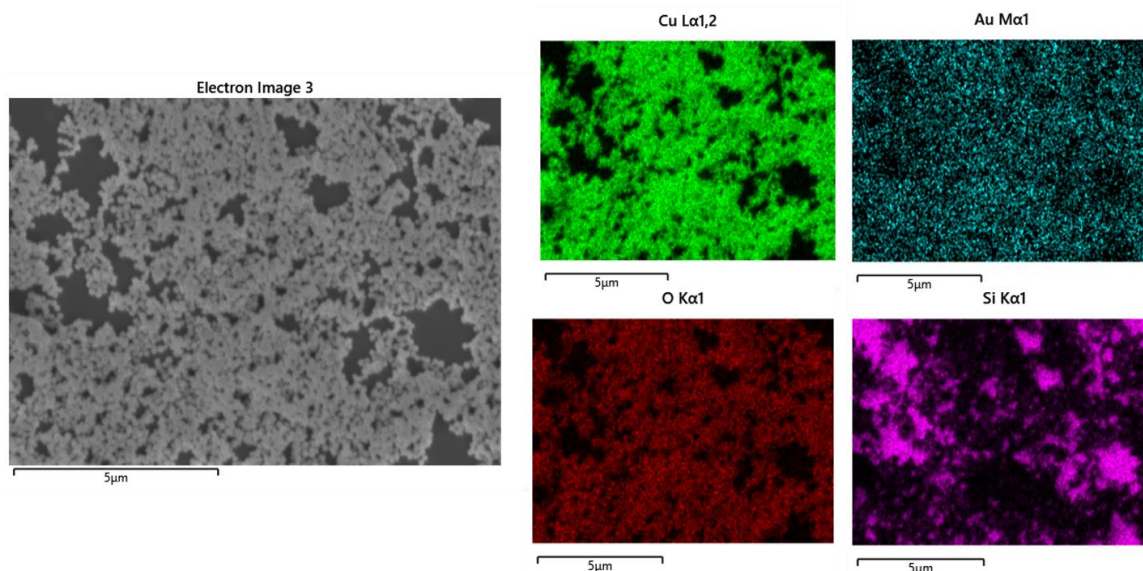
Figure 3. Ap. Analysing the elemental composition of the scaled-up Au decorated Cu2O octahedral NPs. SEM image of the measured area, and the EDS maps of copper, gold, oxygen and silicon.
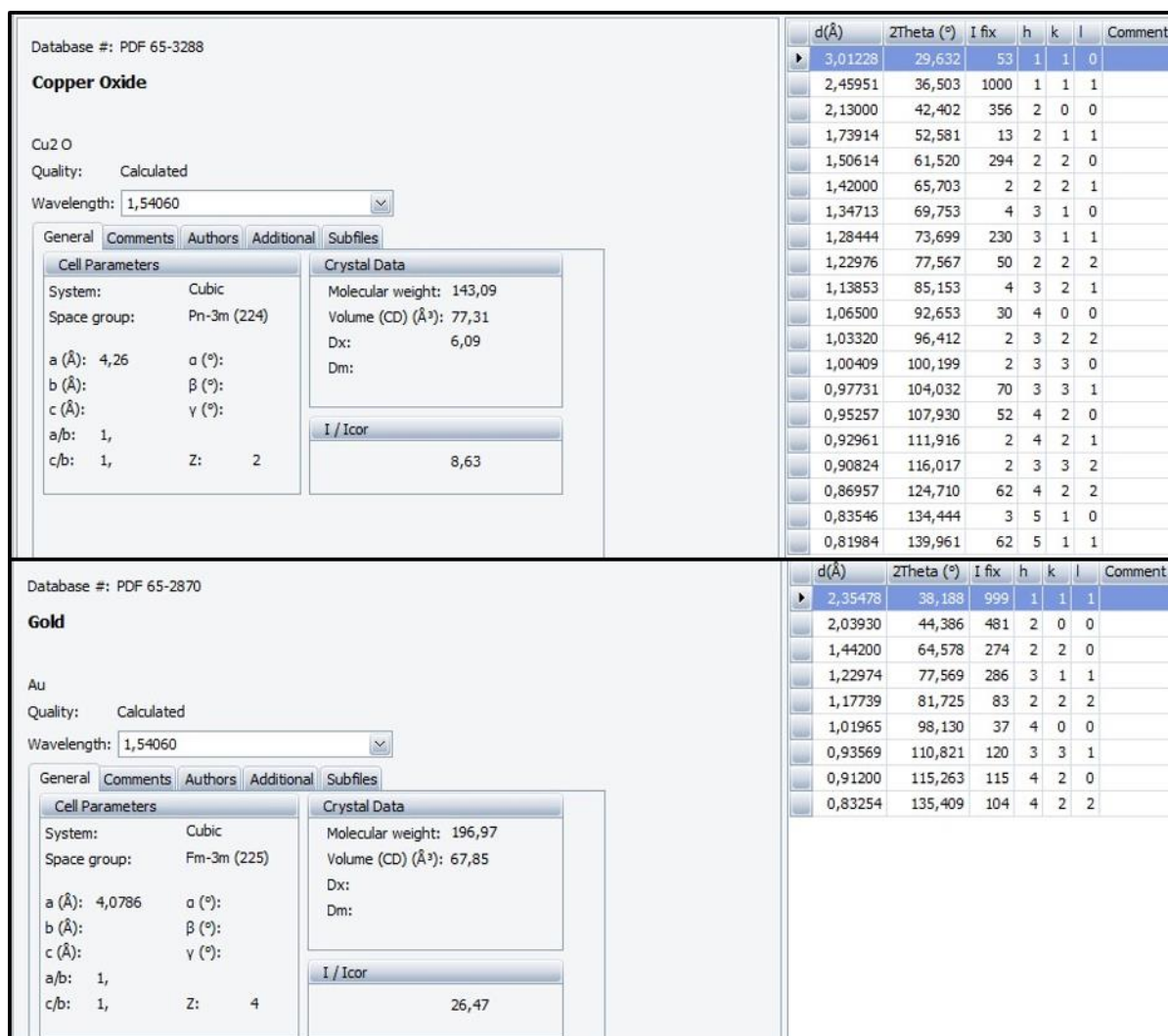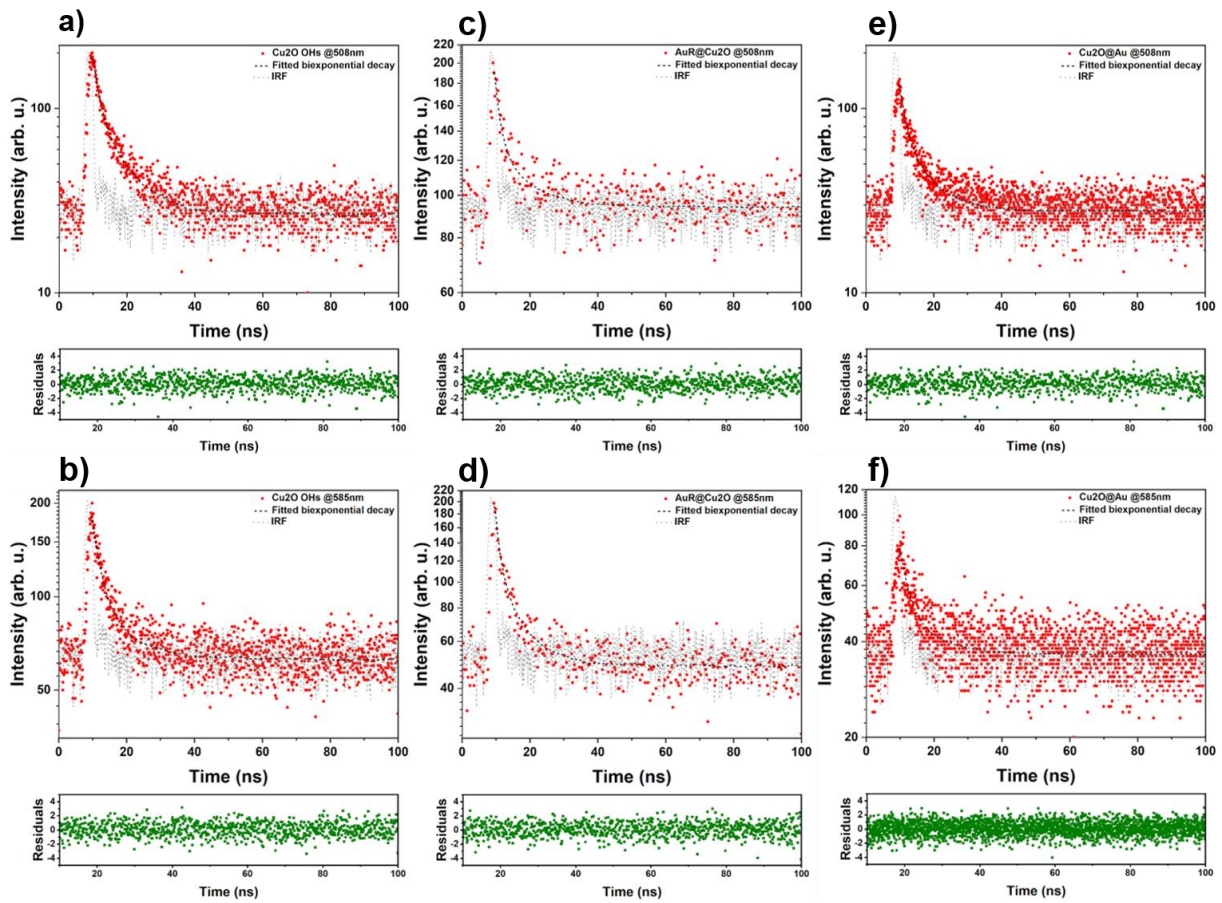

Figure 4. Ap. XRD data cards of Cu_2O and Au.

Figure 5. Ap. Time-correlated single photon counting measurements of (a, b) pristine Cu$_2$O nano octahedra, (c, d) AuNR@Cu$_2$O and (e, f) Cu$_2$O@Au at an excitation wavelength of (a, c, e) 508 nm and (b, d, f) 585 nm. The copper concentration was 0.5 mM (0.0318 g/L) in all samples.
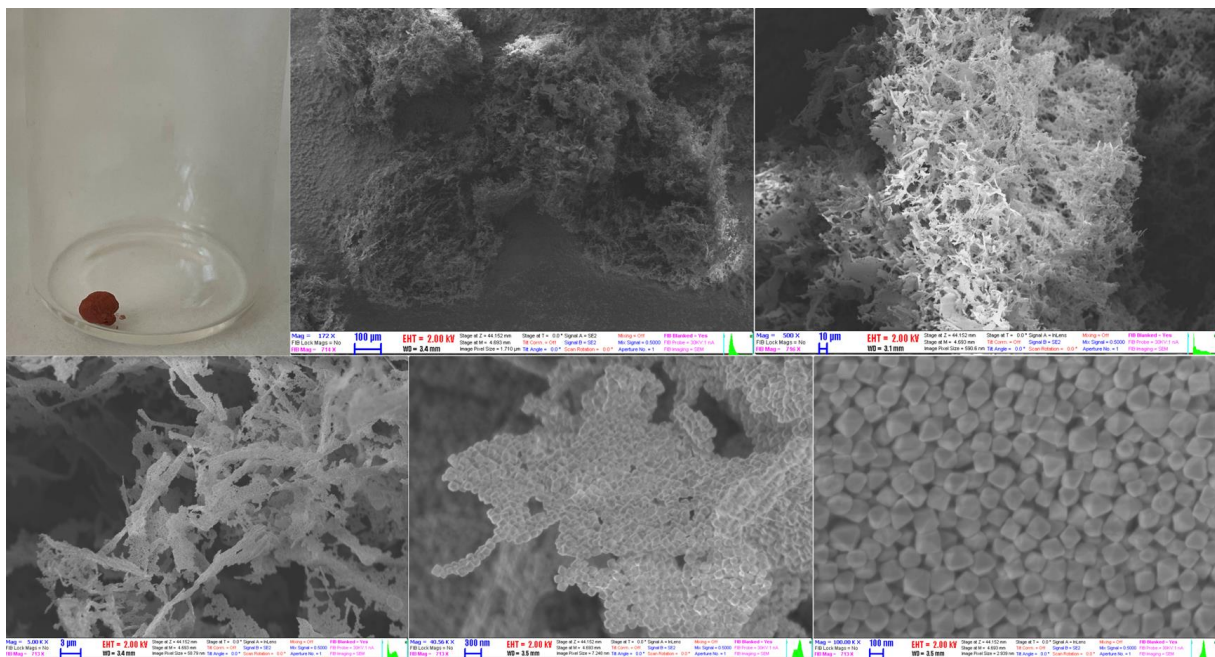

Figure 6. Ap. Cryogelation using pristine Cu$_2$O octahedral NPs. The product and representative SEM images with different magnifications.
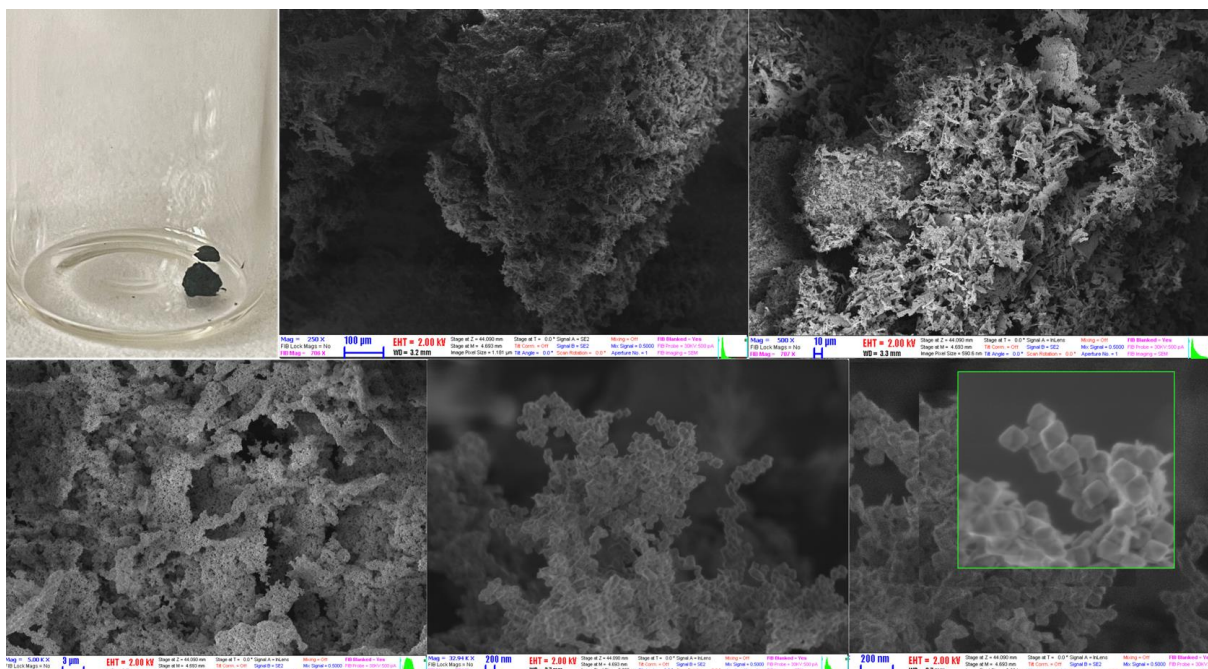
Figure 7. Ap. Cryogelation using AuNR@Cu₂O octahedral NPs. The product and representative SEM images with different magnifications.
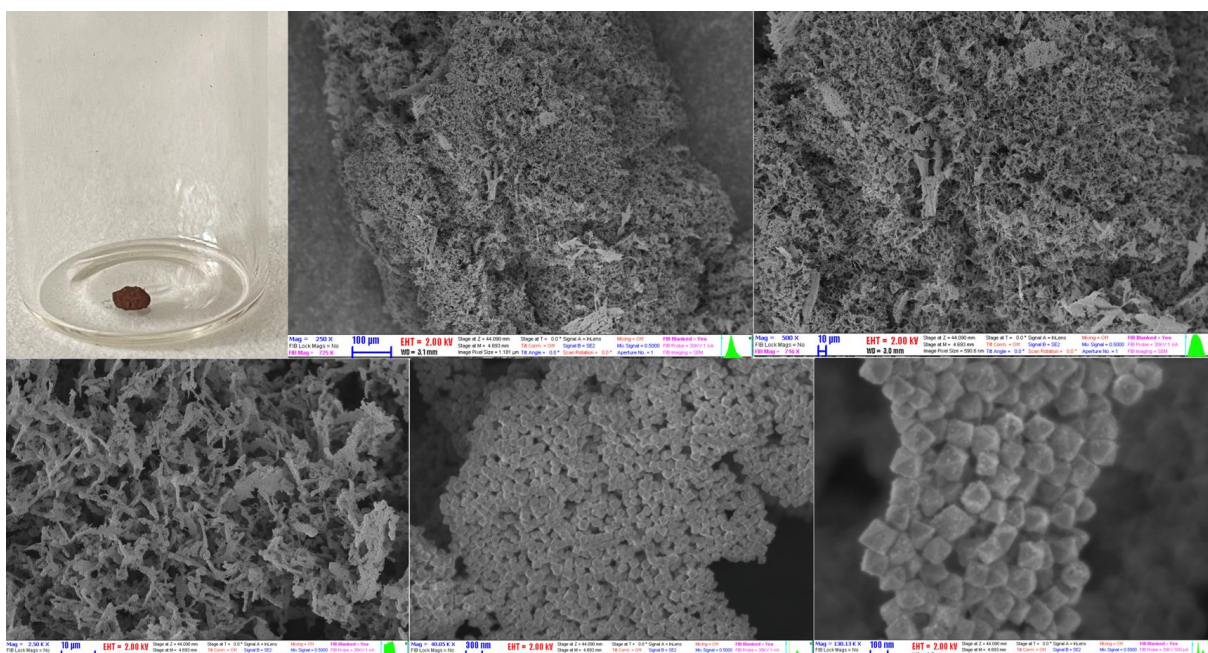

Figure 8. Ap. Cryogelation using Au nanograin decorated Cu₂O octahedral NPs. The product and representative SEM images with different magnifications.

NYILATKOZAT

Név: Kovács Dávid

ELTE Természettudományi Kar, szak: Anyagtudomány MSc

NEPTUN azonosító: OM81T1

Diplomamunka címe:
Multicomponent Copper(I) Oxide/Gold Nanoparticles and Their Assembly

A **diplomamunka** szerzőjeként fegyelmi felelősségem tudatában kijelentem, hogy a dolgozatom önálló szellemi alkotásom, abban a hivatkozások és idézések standard szabályait következetesen alkalmaztam, mások által írt részeket a megfelelő idézés nélkül nem használtam fel.

Budapest, 2022.06.01

_____

a hallgató aláírása